

Banner appropriate to article type will appear here in typeset article

1 A revised gap-averaged Floquet analysis of Faraday 2 waves in Hele-Shaw cells

3 Alessandro Bongarzone¹†, Baptiste Jouron, Francesco Viola² and François
4 Gallaire¹

5 ¹Laboratory of Fluid Mechanics and Instabilities, École Polytechnique Fédérale de Lausanne, Lausanne,
6 CH-1015, Switzerland

7 ²Gran Sasso Science Institute, Viale F. Crispi, 7, 67100 L'Aquila, Italy

8 (Received xx; revised xx; accepted xx)

9 Existing theoretical analyses of Faraday waves in Hele-Shaw cells rely on the Darcy
10 approximation and assume a parabolic flow profile in the narrow direction. However, Darcy's
11 model is known to be inaccurate when convective or unsteady inertial effects are important. In
12 this work, we propose a gap-averaged Floquet theory accounting for inertial effects induced
13 by the unsteady terms in the Navier-Stokes equations, a scenario that corresponds to a
14 pulsatile flow where the fluid motion reduces to a two-dimensional oscillating Poiseuille
15 flow, similarly to the Womersley flow in arteries. When gap-averaging the linearized Navier-
16 Stokes equation, this results in a modified damping coefficient, which is a function of the ratio
17 between the Stokes boundary layer thickness and the cell's gap, and whose complex value
18 depends on the frequency of the wave response specific to each unstable parametric region.
19 We first revisit the standard case of horizontally infinite rectangular Hele-Shaw cells by also
20 accounting for a dynamic contact angle model. A comparison with existing experiments
21 shows the predictive improvement brought by the present theory and points out how the
22 standard gap-averaged model often underestimates the Faraday threshold. The analysis is
23 then extended to the less conventional case of thin annuli. A series of dedicated experiments
24 for this configuration highlights how Darcy's thin-gap approximation overlooks a frequency
25 detuning that is essential to correctly predict the locations of the Faraday tongues in the
26 frequency-amplitude parameter plane. These findings are well rationalized and captured by
27 the present model.

28 1. Introduction

29 Recent Hele-Shaw cell experiments have enriched the knowledge of Faraday waves (Faraday
30 1831). Researchers have uncovered a new type of highly localized standing waves, referred
31 to as oscillons, that are both steep and solitary-like in nature (Rajchenbach *et al.* 2011). These
32 findings have spurred further experimentations with Hele-Shaw cells filled with one or more
33 liquid layers, using a variety of fluids, ranging from silicone oil, and water-ethanol mixtures to
34 pure ethanol (Li *et al.* 2018b). Through these experiments, new combined patterns produced
35 by triadic interactions of oscillons were discovered by Li *et al.* (2014). Additionally, another
36 new family of waves was observed in a cell filled solely with pure ethanol and at extremely

† Email address for correspondence: alessandro.bongarzone@epfl.ch

37 shallow liquid depths (Li *et al.* 2015, 2016).

38 All these findings contribute to the understanding of the wave behaviour in Hele-Shaw
39 configurations and call for a reliable stability theory that can explain and predict the instability
40 onset for the emergence of initial wave patterns.

41 Notwithstanding two-dimensional direct numerical simulations (Périnet *et al.* 2016; Ubal
42 *et al.* 2003) have been able to qualitatively replicate standing wave patterns reminiscent of
43 those observed in experiments (Li *et al.* 2014), these simulations overlook the impact of
44 wall attenuation, hence resulting in a simplified model that cannot accurately predict the
45 instability regions (Benjamin & Ursell 1954; Kumar & Tuckerman 1994) and is therefore
46 not suitable for modelling Hele-Shaw flows. On the other hand, attempting to conduct three-
47 dimensional simulations of fluid motions in a Hele-Shaw cell poses a major challenge due to
48 the high computational cost associated with the narrow dimension of the cell, which requires
49 a smaller grid cell size to capture the shear dissipation accurately. Consequently, the cost of
50 performing such simulations increases rapidly as the cell gap narrows.

51 In order to tackle the challenges associated with resolving fluid dynamics within such
52 systems, researchers have utilized Darcy's law as an approach to treating the confined fluid
53 between two vertical walls. This approximation, also used in the context of porous medium,
54 considers the fluid to be flowing through a porous medium, resulting in a steady parabolic
55 flow in the short dimension. When gap-averaging the linearized Navier-Stokes equation, this
56 approximation translates into a damping coefficient σ that scales as $12\nu/b^2$, with ν the fluid
57 kinematic viscosity and b the cell's gap-size, which represents the boundary layer dissipation
58 at the lateral walls. However, Darcy's model is known to be inaccurate when convective and
59 unsteady inertial effects are not negligible, such as in waves (Kalogirou *et al.* 2016). It is
60 challenging to reintroduce convective terms consistently into the gap-averaged Hele-Shaw
61 equations from a mathematical standpoint (Ruyer-Quil 2001; Plouraboué & Hinch 2002;
62 Luchini & Charru 2010).

63 In their research, Li *et al.* (2019) applied the Kelvin-Helmholtz-Darcy theory proposed by
64 Gondret & Rabaud (1997) to reintroduce advection and derive the nonlinear gap-averaged
65 Navier-Stokes equations. These equations were then implemented in the open-source code
66 *Gerris* developed by Popinet (2003, 2009) to simulate Faraday waves in a Hele-Shaw cell.
67 Although this gap-averaged model was compared to several experiments and demonstrated
68 fairly good agreement, it should be noted that the surface tension term remains two-
69 dimensional, as the out-of-plane interface shape is not directly taken into account. This
70 simplified treatment neglects the contact line dynamics and may lead to miscalculations in
71 certain situations. Advances in this direction were made by Li *et al.* (2018a), who found that
72 the out-of-plane capillary forces associated with the meniscus curvature across the thin-gap
73 direction should be retained in order to improve the description of the wave dynamics, as
74 experimental evidence suggests. By employing a more sophisticated model, coming from
75 molecular kinetics theory (Blake 1993; Hamraoui *et al.* 2000; Blake 2006) and similar to the
76 macroscopic one introduced by Hocking (1987), to include the capillary contact line motion
77 arising from the small scale of the gap-size between the two walls of a Hele-Shaw cell,
78 they derived a novel dispersion relation, which indeed better predicts the observed instability
79 onset.

80 However, discrepancies in the instability thresholds were still found. This mismatch was
81 tentatively attributed to factors that are not accounted for in the gap-averaged model, such
82 as the extra dissipation on the lateral walls in the elongated direction. Of course, a lab-scale
83 experiment using a rectangular cell cannot entirely replace an infinite-length model, but if the
84 container is sufficiently long, then this extra dissipation should be negligible. Other candidates
85 for the mismatch between theory and experiments were identified in the phenomenological
86 contact line model or free surface contaminations.

If these factors can certainly be sources of discrepancies, we believe that a pure hydrodynamic effect could be at the origin of the discordance between theory and experiments in the first place.

Despite the use of the Darcy approximation is well-assessed in the literature, the choice of a steady Poiseuille flow profile as an ansatz to build the gap-averaged model appears in fundamental contrast with the unsteady nature of oscillatory Hele-Shaw flows, such as Faraday waves. At low enough oscillation frequencies or for sufficiently viscous fluids, the thickness of the oscillating Stokes boundary layer becomes comparable to the cell gap: the Stokes layers over the lateral solid faces of the cell merge and eventually invade the entire fluid bulk. In such scenarios, the Poiseuille profile gives an adequate flow description, but this pre-requisite is rarely met in the above-cited experimental campaigns. It appears, thus, very natural to ask oneself whether a more appropriate description of the oscillating boundary layer impacts the prediction of stability boundaries. This study is precisely devoted to answering this question by proposing a revised gap-averaged Floquet analysis, based on the classical Womersley-like solution for the pulsating flow in a channel (Womersley 1955; San & Staples 2012).

Following the approach taken by Viola *et al.* (2017), we examine the impact of inertial effects on the instability threshold of Faraday waves in Hele-Shaw cells, with a focus on the unsteady term of the Navier-Stokes equations. This scenario corresponds to a pulsatile flow where the fluid's motion reduces to a two-dimensional oscillating channel flow, which seems better suited than the steady Poiseuille profile to investigate the stability properties of the system. When gap-averaging the linearized Navier-Stokes equation, this results in a modified damping coefficient becoming a function of the ratio between the Stokes boundary layer thickness and the cell's gap, and whose complex value will depend on the frequency of the wave response specific to each unstable parametric region.

First, we consider the case of horizontally infinite rectangular Hele-Shaw cells by also accounting for the same dynamic contact angle model employed by Li *et al.* (2019), so as to quantify the predictive improvement brought by the present theory. A *vis-à-vis* comparison with experiments by Li *et al.* (2019) points out how the standard Darcy model often underestimates the Faraday threshold, whereas the present theory can explain and close the gap with these experiments.

The analysis is then extended to the case of thin annuli. This less common configuration has been already used to investigate oscillatory phase modulation of parametrically forced surface waves (Douady *et al.* 1989) and drift instability of cellular patterns (Fauve *et al.* 1991). For our interest, an annular cell is convenient as it naturally filters out the extra dissipation that could take place on the lateral boundary layer in the elongated direction, hence allowing us to reduce the sources of extra uncontrolled dissipation and perform a cleaner comparison with experiments. Our homemade experiments for this configuration highlight how Darcy's theory overlooks a frequency detuning that is essential to correctly predict the locations of the Faraday's tongues in the frequency spectrum. These findings are well rationalized and captured by the present model.

The paper is organized as follows. In §2 we revisit the classical case of horizontally infinite rectangular Hele-Shaw cells. The present model is compared with theoretical predictions from the standard Darcy theory and with existing experiments. The case of thin annuli is then considered. The model for the latter unusual configuration is formulated in §3 and compared with homemade experiments in §4. Conclusions are outlined in §5.

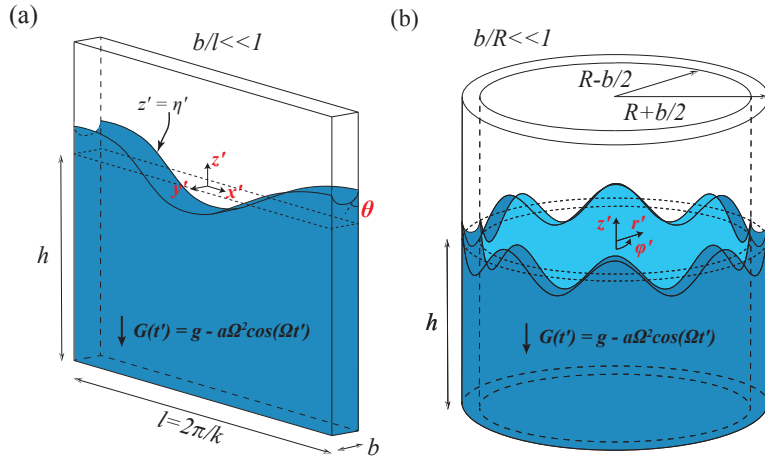


Figure 1: (a) Sketch of Faraday waves in a rectangular Hele-Shaw cell of width b and length l filled to a depth h with a liquid. Here b denotes the gap size of the Hele-Shaw cell, l is the wavelength of a certain wave, such that $b/l \ll 1$, and θ is the dynamic contact angle of the liquid on the lateral walls. The vessel undergoes a vertical sinusoidal oscillation of amplitude a and angular frequency Ω . The free surface elevation is denoted by $\eta'(x')$. (b) Same as (a), but in an annular Hele-Shaw cell with internal and external radii, respectively, $R - b/2$ and $R + b/2$. Here, $b/R \ll 1$ and the free surface elevation is a function of the azimuthal coordinate φ' , i.e. $\eta'(\varphi')$.

2. Horizontally infinite Hele-Shaw cells

Let us begin by considering the case of a horizontally infinite Hele-Shaw cell of width b filled to a depth h with an incompressible fluid of density ρ , dynamic viscosity μ (kinematic viscosity $\nu = \mu/\rho$) and liquid-air surface tension γ (see also sketch in figure 1(a)). The vessel undergoes a vertical sinusoidal oscillation of amplitude a and angular frequency Ω . In a frame of reference which moves with the oscillating container, the free liquid interface is flat and stationary for small forcing amplitudes, and the oscillation is equivalent to a temporally modulated gravitational acceleration, $G(t') = g - a\Omega^2 \cos \Omega t'$. The equation of motion for the fluid bulk are

$$\rho \left(\frac{\partial \mathbf{U}'}{\partial t'} + \mathbf{U}' \cdot \nabla' \mathbf{U}' \right) = -\nabla' P' + \mu \nabla'^2 \mathbf{U}' - \rho G(t) \mathbf{e}_z, \quad \nabla' \cdot \mathbf{U}' = 0. \quad (2.1)$$

Linearizing about the rest state $\mathbf{U}' = \mathbf{0}$ and $P'(z', t') = -\rho G(t) z'$, the equations for the perturbation velocity, $\mathbf{u}'(x', y', z', t') = \{u', v', w'\}^T$, and pressure, $p'(x', y', z', t')$, fields, associated with a certain perturbation's wavelength $l = 2\pi/k$ (k , wavenumber), read

$$\rho \frac{\partial \mathbf{u}'}{\partial t'} = -\nabla' p' + \mu \nabla'^2 \mathbf{u}', \quad \nabla' \cdot \mathbf{u}' = 0. \quad (2.2)$$

Assuming that $bk \ll 1$, then the velocity along the narrow y' -dimension $v' \ll u', w'$ and, by employing the Hele-Shaw approximation as in, for instance, Viola *et al.* (2017), one can simplify the linearized Navier-Stokes equations as follows:

$$\frac{\partial u'}{\partial x'} + \frac{\partial v'}{\partial y'} + \frac{\partial w'}{\partial z'} = 0, \quad (2.3a)$$

151 $\rho \frac{\partial u'}{\partial t'} = -\frac{\partial p'}{\partial x'} + \mu \frac{\partial^2 u'}{\partial y'^2}, \quad \rho \frac{\partial w'}{\partial t'} = -\frac{\partial p'}{\partial z'} + \mu \frac{\partial^2 w'}{\partial y'^2}, \quad \frac{\partial p'}{\partial y'} = 0. \quad (2.3b)$

152 Equations (2.3a)-(2.3b) are made dimensionless using k^{-1} for the directions x' and z' , and b
153 for y' . The forcing amplitude and frequency provide a scale $a\Omega$ for the in-plane xz -velocity
154 components, whereas the continuity equation imposes the transverse component v' to scale
155 as $v' \sim bka\Omega \ll a\Omega \sim u'$, due to the strong confinement in the y -direction ($bk \ll 1$). With
156 these choices, dimensionless spatial scales, velocity components and pressure write:

157 $x = x'k, \quad y = \frac{y'}{b}, \quad z = z'k, \quad u = \frac{u'}{a\Omega}, \quad v = \frac{v'}{bka\Omega}, \quad w = \frac{w'}{a\Omega}, \quad p = \frac{kp'}{\rho a\Omega^2}, \quad t = \Omega t'. \quad (2.4)$

158 The first two equations in (2.3b) in non-dimensional form are

159 $\frac{\partial u}{\partial t} = -\frac{\partial p}{\partial x} + \frac{\delta_{St}^2}{2} \frac{\partial^2 u}{\partial y^2}, \quad \frac{\partial w}{\partial t} = -\frac{\partial p}{\partial z} + \frac{\delta_{St}^2}{2} \frac{\partial^2 w}{\partial y^2}, \quad (2.5)$

160 where $\delta_{St} = \delta'_{St}/b$ and with $\delta'_{St} = \sqrt{2\nu/\Omega}$ denoting the thickness of the oscillating Stokes
161 boundary layer. The ratio $\sqrt{2}/\delta_{St}$ is also commonly referred to as the Womersley number,
162 $Wo = b\sqrt{\Omega/\nu}$ (Womersley 1955; San & Staples 2012).

163 2.1. Floquet analysis of the gap-averaged equations

164 Given its periodic nature, the stability of the base flow, represented by a time-periodic
165 modulation of the hydrostatic pressure, can be investigated via Floquet analysis. We therefore
166 introduce the following Floquet ansatz (Kumar & Tuckerman 1994)

167 $\mathbf{u}(x, y, z, t) = e^{\mu_F t} \sum_{n=-\infty}^{+\infty} \tilde{\mathbf{u}}_n(x, y, z) e^{i(n+\alpha/\Omega)t} = e^{\mu_F t} \sum_{n=-\infty}^{+\infty} \tilde{\mathbf{u}}_n(x, y, z) e^{i\xi_n t}, \quad (2.6a)$

168

169 $p(x, z, t) = e^{\mu_F t} \sum_{n=-\infty}^{+\infty} \tilde{p}_n(x, z) e^{i(n+\alpha/\Omega)t} = e^{\mu_F t} \sum_{n=-\infty}^{+\infty} \tilde{p}_n(x, z) e^{i\xi_n t}, \quad (2.6b)$

170 where μ_F is the real part of the non-dimensional Floquet exponent and represents the growth
171 rate of the perturbation. We have rewritten $(n + \alpha/\Omega) = \xi_n$ to better explicit the parametric
172 nature of the oscillation frequency of the wave response. In the following, we will focus
173 on the condition for marginal stability (boundaries of the Faraday's tongues), which require
174 the growth rate $\mu_F = 0$. In addition, values of $\alpha = 0$ and $\Omega/2$ correspond, respectively, to
175 harmonic and sub-harmonic parametric resonances (Kumar & Tuckerman 1994). This implies
176 that ξ_n is a parameter whose value is either n , for harmonics, or $n + 1/2$, for sub-harmonics,
177 with n an integer $n = 0, 1, 2, \dots$ specific to each Fourier component in (2.6a)-(2.6b).

178 By injecting the ansatzs (2.6a)-(2.6b) in (2.5), we find that each component of the Fourier
179 series must satisfy

180 $\forall n : \quad i\xi_n \tilde{u}_n = -\frac{\partial \tilde{p}_n}{\partial x} + \frac{\delta_{St}^2}{2} \frac{\partial^2 \tilde{u}_n}{\partial y^2}, \quad i\xi_n \tilde{w}_n = -\frac{\partial \tilde{p}_n}{\partial z} + \frac{\delta_{St}^2}{2} \frac{\partial^2 \tilde{w}_n}{\partial y^2}, \quad (2.7)$

181 which, along with the no-slip condition at $y = \pm 1/2$, correspond to a two-dimensional
182 pulsatile Poiseuille flow with solution

183 $\tilde{u}_n = \frac{i}{\xi_n} \frac{\partial \tilde{p}_n}{\partial x} F_n(y), \quad \tilde{w}_n = \frac{i}{\xi_n} \frac{\partial \tilde{p}_n}{\partial z} F_n(y), \quad F_n(y) = \left(1 - \frac{\cosh(1+i)y/\delta_n}{\cosh(1+i)/2\delta_n}\right), \quad (2.8)$

184 and where $\delta_n = \delta_{St}/\sqrt{\xi_n}$, is a rescaled Stokes boundary layer thickness specific to the n th
185 Fourier component. The function $F_n(y)$ is displayed in figure 2(b), which depicts how a

decrease in the value of δ_n starting from large values corresponds to a progressive transition from a fully developed flow profile to a plug flow connected to thin boundary layers.

The gap-averaged velocity along the y -direction satisfies a Darcy-like equation,

$$\langle \tilde{\mathbf{u}}_n \rangle = \int_{-1/2}^{1/2} \tilde{\mathbf{u}}_n dy = \frac{i\beta_n}{\xi_n} \nabla \tilde{p}_n, \quad \beta_n = 1 - \frac{2\delta_n}{1+i} \tanh \frac{1+i}{2\delta_n}. \quad (2.9)$$

In order to obtain a governing equation for the pressure \tilde{p}_n , we average the continuity equation and we impose the impermeability condition for the spanwise velocity, $v = 0$ at $y = \pm 1/2$,

$$\frac{\partial \langle \tilde{u}_n \rangle}{\partial x} + \underbrace{\int_{-1/2}^{1/2} \frac{\partial \tilde{v}_n}{\partial y} dy}_{\tilde{v}_n(1/2) - \tilde{v}_n(-1/2)=0} + \frac{\partial \langle \tilde{w}_n \rangle}{\partial z} = \nabla \cdot \langle \tilde{\mathbf{u}}_n \rangle = 0, \quad (2.10)$$

Since $\langle \tilde{\mathbf{u}}_n \rangle = i(\beta_n/\xi_n) \nabla \tilde{p}_n$, the pressure field \tilde{p}_n must obey the Laplace equation

$$\nabla^2 \tilde{p}_n = \frac{\partial^2 \tilde{p}_n}{\partial x^2} + \frac{\partial^2 \tilde{p}_n}{\partial z^2} = 0. \quad (2.11)$$

It is now useful to expand each Fourier component $\tilde{p}_n(x, z)$ in the infinite x -direction as $\sin x$ such that the y -average implies,

$$\tilde{p}_n(x, z) = \hat{p}_n(z) \sin x, \quad (2.12a)$$

$$\langle \tilde{u}_n \rangle = \hat{u}_n = \frac{i\beta_n}{\xi_n} \hat{p}_n \cos x, \quad \langle \tilde{w}_n \rangle = \hat{w}_n = \frac{i\beta_n}{\xi_n} \frac{\partial \hat{p}_n}{\partial z} \sin x. \quad (2.12b)$$

Replacing (2.12a) in (2.11) leads to

$$\left(\frac{\partial^2}{\partial z^2} - 1 \right) \hat{p}_n = 0, \quad (2.13)$$

which admits the solution form

$$\hat{p}_n = c_1 \cosh z + c_2 \sinh z. \quad (2.14)$$

The presence of a solid bottom imposes that $\hat{w}_n = 0$ and, therefore, that $\partial \hat{p}_n / \partial z = 0$, at a non-dimensional fluid depth $z = -hk$, hence giving

$$\hat{p}_n = c_1 [\cosh z + \tanh kh \sinh z]. \quad (2.15)$$

Let us now invoke the linearized kinematic boundary condition

$$\frac{\partial \eta}{\partial t} = w. \quad (2.16)$$

Note that free surface elevation, $\eta'(x', y', t')$, has been rescaled by the forcing amplitude a , i.e. $\eta'/a = \eta$, and represents the projection of the bottom of the transverse concave meniscus on the xz -plane of figure 1(a). Moreover, by recalling the Floquet ansatzs (2.6a)-(2.6b) (with $\mu_F = 0$), here specified for the interface, we get an equation for each Fourier component n ,

$$\eta = \sum_{n=-\infty}^{+\infty} \tilde{\eta}_n e^{i\xi_n t} \quad \longrightarrow \quad \forall n : \quad i\xi_n \tilde{\eta}_n = \tilde{w}_n. \quad (2.17)$$

Expanding $\tilde{\eta}_n$ in the x -direction as $\sin x$ and averaging in y , i.e. $\langle \tilde{\eta}_n \rangle = \hat{\eta}_n \sin x$, leads to

$$i\xi_n \hat{\eta}_n = \hat{w}_n = \frac{i\beta_n}{\xi_n} \frac{\partial \hat{p}_n}{\partial z} \Big|_{z=0} = \frac{i\beta_n}{\xi_n} c_1 \tanh kh \quad \longrightarrow \quad c_1 = \frac{\xi_n^2}{\beta_n} \frac{\hat{\eta}_n}{\tanh kh}. \quad (2.18)$$

216 Lastly, we consider the linearized dynamic condition (or linearized normal stress), evaluated
 217 at $z' = \eta'$ and where the term associated with the curvature of the free surface appears,

$$218 \quad -p' + \rho G(t')\eta' + 2\mu \frac{\partial w'}{\partial z'} - \gamma \left. \frac{\partial \kappa'}{\partial \eta'} \right| \eta' = 0. \quad (2.19)$$

219 In (2.19), $\partial \kappa'/\partial \eta'$ represents the first-order variation of the curvature associated with the
 220 small perturbation η' . Capillary force in the x -direction is only important at large enough
 221 wavenumbers, although the associated term can be retained in the analysis in order to retrieve
 222 the dispersion relation for capillary-gravity waves (Li *et al.* 2019). On the other hand, the
 223 small gap of Hele-Shaw cells is such that surface tension effects in the narrow y -direction
 224 are strongly exacerbated. In general, the curvature can be divided into two parts (Saffman &
 225 Taylor 1958; Chuoke *et al.* 1959):

$$226 \quad \kappa'(\eta') = \frac{\partial}{\partial x'} \left(\frac{\partial_{x'} \eta'}{\sqrt{1 + (\partial_{x'} \eta')^2}} \right) + \frac{2}{b} \cos \theta, \quad (2.20)$$

227 where the first term indicates the principal radius of curvature and the second term represents
 228 the out-of-plane curvature of the meniscus (see figure 1(a)). A common treatment of
 229 Hele-Shaw cells assumes the out-of-plane interface shape to be semicircular (Saffman &
 230 Taylor 1958; McLean & Saffman 1981; Park & Homsy 1984; Afkhami & Renardy 2013).
 231 Nevertheless, laboratory observations have unveiled that liquid oscillations in Hele-Shaw
 232 cells experience an up-and-down driving force with θ constantly changing (Jiang *et al.*
 233 2004), hence giving rise to a dynamic contact angle. Here, as in Li *et al.* (2019), we use the
 234 following model (Hamraoui *et al.* 2000) to evaluate the cosine of the dynamic contact angle
 235 θ as

$$236 \quad \cos \theta = 1 - \frac{M}{\mu} Ca = 1 - \frac{Mw'}{\gamma} \quad (2.21)$$

237 where $Ca = \mu w'/\gamma$ is the Capillary number defined using the vertical contact line velocity
 238 $w' = \partial \eta'/\partial t'$. The friction coefficient M , sometimes referred to as mobility parameter
 239 M (Xia & Steen 2018), can be interpreted in the framework of molecular kinetics theory
 240 (O. V. Voinov 1976; Hocking 1987; Blake 1993, 2006; Johansson & Hess 2018). Here, we
 241 simply view this coefficient as a constant phenomenological parameter that defines the energy
 242 dissipation rate per unit length of the contact line and, as in Li *et al.* (2019), we directly use
 243 the values employed by Hamraoui *et al.* (2000).

244 By combining equations (2.20)-(2.21) and taking their first-order curvature variation
 245 applied to the small perturbation, one can express

$$246 \quad -\gamma \left. \frac{\partial \kappa'}{\partial \eta'} \right| \eta' = -\gamma \frac{\partial^2 \eta'}{\partial x'^2} + \frac{2M}{b} \frac{\partial \eta'}{\partial t'}. \quad (2.22)$$

247 After turning to non-dimensional quantities using the scaling in (2.4), equations (2.19) reads

$$248 \quad -\Omega^2 p + g\eta - \frac{\gamma}{\rho} k^2 \frac{\partial^2 \eta}{\partial x^2} + \frac{2M}{\rho b} \Omega \frac{\partial \eta}{\partial t} = a\Omega^2 \cos t\eta, \quad (2.23)$$

249 where the viscous stress term has been eliminated, as it is negligible compared to the others.

250 With introduction of the Floquet ansatz (2.6b)-(2.17) and by recalling the x -expansion of
 251 the interface and pressure as $\sin x$, the averaged normal stress equations become

$$252 \quad \forall n : -\Omega^2 \hat{p}_n + i(\xi_n \Omega) \frac{2M}{\rho b} \hat{\eta}_n + \left(1 + \frac{\gamma}{\rho g} k^2 \right) g \hat{\eta}_n = \frac{a\Omega^2}{2g} g (\hat{\eta}_{n-1} + \hat{\eta}_{n+1}). \quad (2.24)$$

253 where the decomposition $\cos \Omega t' = (e^{i\Omega t'} + e^{-i\Omega t'}) / 2 = (e^{it} + e^{-it}) / 2$ has also been used.
 254 Equations (2.15) and (2.18) are finally used to express the dynamic equation as a function of
 255 the non-dimensional averaged interface only,

$$256 - \frac{(\xi_n \Omega)^2}{\beta_n} \hat{\eta}_n + i(\xi_n \Omega) \frac{2M}{\rho b} k \tanh kh \hat{\eta}_n + (1 + \Gamma) gk \tanh kh \hat{\eta}_n = \frac{gk \tanh kh}{2} f(\hat{\eta}_{n-1} + \hat{\eta}_{n+1}), \quad (2.25)$$

257 with the auxiliary variables $f = a\Omega^2/g$ and $\Gamma = \gamma k^2/\rho g$, such that $(1 + \Gamma) gk \tanh kh = \omega_0^2$,
 258 the well-known dispersion relation for capillary-gravity waves (Lamb 1993).

259 As in the present form the interpretation of coefficient β_n does not appear straightforward,
 260 it is useful to define the damping coefficients

$$261 \sigma_n = \sigma_{BL} + \sigma_{CL}, \quad \sigma_{BL} = \chi_n \frac{v}{b^2}, \quad \sigma_{CL} = \frac{2M}{\rho b} k \tanh kh, \quad (2.26a)$$

262 where χ_n is used to help rewriting $\frac{1}{\beta_n} = 1 - i\frac{\delta_n^2}{2} \chi_n$,

$$263 \chi_n = i \frac{2}{\delta_n^2} \left(\frac{1 - \beta_n}{\beta_n} \right) = 12 \left[\frac{i}{6\delta_n^2} \left(\frac{\frac{2\delta_n}{1+i} \tanh \frac{1+i}{2\delta_n}}{1 - \frac{2\delta_n}{1+i} \tanh \frac{1+i}{2\delta_n}} \right) \right]. \quad (2.26b)$$

264 These auxiliary definitions allows one to express (2.25) as

$$265 - (\xi_n \Omega)^2 \hat{\eta}_n + i(\xi_n \Omega) \sigma_n \hat{\eta}_n + \omega_0^2 \hat{\eta}_n = \frac{\omega_0^2}{2(1 + \Gamma)} f [\hat{\eta}_{n+1} + \hat{\eta}_{n-1}]. \quad (2.27)$$

266 or, equivalently,

$$267 \frac{2(1 + \Gamma)}{\omega_0^2} [-(n\Omega + \alpha)^2 + i(n\Omega + \alpha) \sigma_n + \omega_0^2] \hat{\eta}_n = f [\hat{\eta}_{n+1} + \hat{\eta}_{n-1}]. \quad (2.28)$$

268 Subscripts *BL* and *CL* in (2.26a) denote, respectively, the boundary layers and contact line
 269 contributions to the total damping coefficient σ_n .

270 At the end of this mathematical derivation, a useful result is the modified damping
 271 coefficient σ_n . Since the boundary layer contribution, σ_{BL} depends on the *n*th Fourier
 272 component, the overall damping, σ_n , is mode dependent and its value is different for each
 273 specific *n*th parametric resonant tongue considered. This is in stark contrast with the standard
 274 Darcy approximation, where σ_{BL} is the same for each resonance and amounts to $12v/b^2$.
 275 In our model, the case of $\alpha = 0$ with $n = 0$ constitutes a peculiar case, as $\xi_n = \xi_0 = 0$ and
 276 $\delta_0 \rightarrow +\infty$. In such a situation, $F_0(y)$ tends to the steady Poiseuille profile, so that we take
 277 $\chi_0 = 12$.

278 Similarly to Kumar & Tuckerman (1994), equation (2.28) is rewritten as

$$279 A_n \hat{\eta}_n = f [\hat{\eta}_{n+1} + \hat{\eta}_{n-1}], \quad (2.29)$$

280 with

$$281 A_n = \frac{2(1 + \Gamma)}{\omega_0^2} [-(n\Omega + \alpha)^2 + i(n\Omega + \alpha) \sigma_n + \omega_0^2] = A_n^r + iA_n^i \in \mathbb{C} \quad (2.30)$$

282 The non-dimensional amplitude of the external forcing, $f = a\Omega^2/g$ appears linearly,
 283 therefore (2.29) can be considered to be a generalized eigenvalue problem

$$284 \mathbf{A}\hat{\eta} = f\mathbf{B}\hat{\eta}, \quad (2.31)$$

285 with eigenvalues f and eigenvectors whose components are the real and imaginary parts of
 286 $\hat{\eta}_n$. See Kumar & Tuckerman (1994) for the structure of matrices \mathbf{A} and \mathbf{B} .

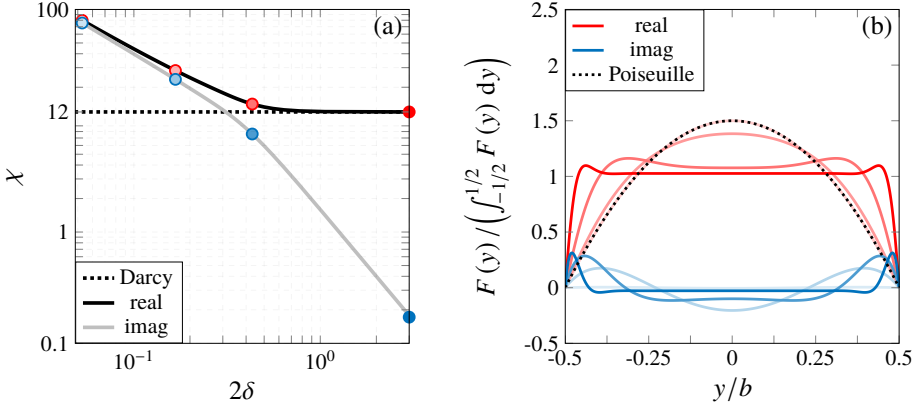


Figure 2: (a) Real and imaginary parts of the complex auxiliary coefficient $\chi = \chi_r + i\chi_i$ versus twice the non-dimensional Stokes boundary layer thickness δ . The horizontal black dotted line indicates the constant value 12 given by the Darcy approximation. (b) Normalized profile $F(y)$ (Womersley profile) for different $\delta = b^{-1}\sqrt{2\nu/\xi\Omega}$, whose values are specified by the filled circles in (a) with matching colors. The Poiseuille profile is also reported for completeness. In drawing these figures we let the oscillation frequency of the wave, $\xi\Omega$, free to assume any value, but we recall that the parameter ξ can only assume discrete values, and so do χ and $F(y)$.

287 For one frequency forcing we use a truncation number $N = 10$, which produces $2(N+1) \times$
 288 $2(N+1) = 22 \times 22$ matrices. Eigen-problem (2.31) is then solved in Matlab using the built-in
 289 function *eigs*. For a fixed forcing frequency Ω and wavenumber k , the eigenvalue with the
 290 smallest real part will define the instability threshold.

291 Figure 3 shows the results of this procedure for one of the configurations considered by Li
 292 *et al.* (2019) and neglecting the dissipation associated with the contact line motion, i.e. $M = 0$.
 293 In each panel, associated with a fixed forcing frequency, the black regions correspond to the
 294 unstable Faraday tongues computed using $\sigma_{BL} = 12\nu/b^2$ as given by Darcy's approximation,
 295 whereas the red regions are the unstable tongues computed with the modified $\sigma_{BL} = \chi_n\nu/b^2$.
 296 At a forcing frequency 4 Hz the first sub-harmonic tongues computed using the two models
 297 essentially overlap. Yet, successive resonances display an increasing departure from Darcy's
 298 model due to the newly introduced complex coefficient σ_n . Particularly, the real part of χ_n
 299 is responsible for the higher onset acceleration, while the imaginary part is expected to act
 300 as a detuning term, which shifts the resonant wavenumbers k .

301 2.2. Asymptotic approximations

302 The main result of this analysis consists in the derivation of the modified damping coefficient
 303 $\sigma_n = \sigma_{n,r} + i\sigma_{n,i}$ associated with each parametric resonance. Aiming at better elucidating
 304 how this modified complex damping influences the stability properties of the system, we
 305 would like to derive in this section an asymptotic approximation, valid in the limit of small
 306 forcing amplitudes, damping and detuning, of the first sub-harmonic (SH1) and harmonic
 307 (H1) Faraday tongues.

308 Unfortunately, the dependence of σ_n on the parametric resonance considered and, more
 309 specifically, on the n th Fourier component, does not allow one to directly convert the gov-
 310 erning equations (2.27), expressed in a discrete frequency domain, back into the continuous
 311 temporal domain. By keeping this in mind, we can still imagine fixing the value of σ_n to that
 312 corresponding to the parametric resonance of interest, e.g. σ_0 (with $n = 0$ and $\xi_0\Omega = \Omega/2$)
 313 for SH1 or σ_1 (with $n = 1$ and $\xi_1\Omega = \Omega$) for H1. By considering then that for the SH1

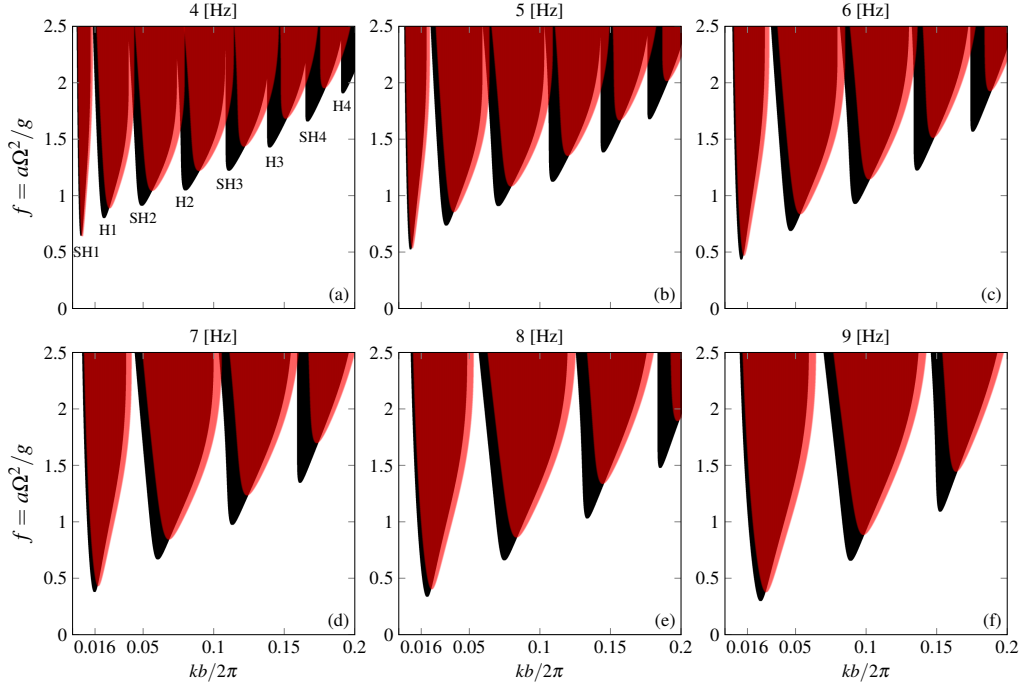


Figure 3: Faraday tongues computed via Floquet analysis at different fixed driving frequencies, $\Omega/2\pi$ (reported on the top of each panel). Black regions correspond to the unstable Faraday tongues computed using $\sigma_{BL} = 12\nu/b^2$ as in the standard Darcy approximation, whereas red regions are the unstable tongues computed with the present modified $\sigma_{BL} = \chi_n \nu/b^2$. For this example, we consider ethanol 99.7% (see table 1) in a Hele-Shaw cell of gap size $b = 2$ mm filled to a depth $h = 60$ mm. f denotes the non-dimensional forcing acceleration, $f = a\Omega^2/g$, with dimensional forcing amplitude a and angular frequency Ω . For plotting, we define a small scale-separation parameter $\epsilon = kb/2\pi$ and we arbitrarily set its maximum acceptable value to 0.2. Contact line dissipation is not included, i.e. $M = \sigma_{CL} = 0$. SH stands for sub-harmonic, whereas H stands for harmonic.

314 and H1 tongues, the system responds in time as $\exp(i\Omega t/2)$ and $\exp(i\Omega t)$, respectively, we
 315 can recast, for these two specific cases, equations (2.27) into a damped Mathieu equation
 316 (Benjamin & Ursell 1954; Kumar & Tuckerman 1994; Müller *et al.* 1997)

$$317 \quad \frac{\partial^2 \hat{\eta}}{\partial t'^2} + \hat{\sigma}_n \frac{\partial \hat{\eta}}{\partial t'} + \omega_0^2 \left(1 - \frac{f}{1 + \Gamma} \cos \Omega t' \right) \hat{\eta} = 0. \quad (2.32)$$

318 with either $\hat{\sigma}_n = \sigma_0$ (SH1) or $\hat{\sigma}_n = \sigma_1$ (H1) and where one can recognize that $-(\xi_n \Omega)^2 \hat{\eta} \leftrightarrow$
 319 $\partial^2 \hat{\eta} / \partial t'^2$ and $i(\xi_n \Omega) \hat{\eta} \leftrightarrow \partial \hat{\eta} / \partial t'$. Asymptotic approximations can be then computed by
 320 expanding asymptotically the interface as $\hat{\eta} = \hat{\eta}_0 + \epsilon \hat{\eta}_1 + \epsilon^2 \hat{\eta}_2 + \dots$, with ϵ a small parameter
 321 $\ll 1$.

322 2.2.1. First sub-harmonic tongue

323 As anticipated above, when looking at the first or fundamental sub-harmonic tongue (SH1),
 324 one should take $\hat{\sigma}_n \rightarrow \sigma_0$ (with $\xi_0 \Omega = \Omega/2$), which is assumed small of order ϵ . The forcing
 325 amplitude f is assumed of order ϵ as well. Furthermore, a small detuning $\sim \epsilon$, such that
 326 $\Omega = 2\omega_0 + \epsilon\lambda$, is also considered, and, in the spirit of the multiple timescale analysis, a
 327 slow time scale $T = \epsilon t'$ (Nayfeh 2008) is introduced. At leading order, the solution reads

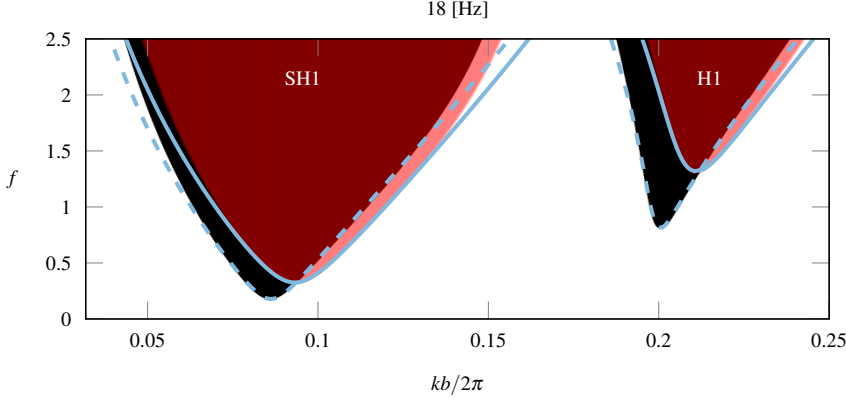


Figure 4: First sub-harmonic and harmonic Faraday tongues at a driving frequency $1/T = 18$ Hz for the same configuration of figure 3. Black and red regions show unstable tongues computed via Floquet analysis by using, respectively, $\sigma_{BL} = 12v/b^2$ and the modified $\sigma_{BL} = \chi_1 v/b^2$ from the present model. Dashed and solid light-blue lines correspond to the asymptotic approximations according to (2.34) and (2.37).

328 $\hat{\eta}_0 = A(T) e^{i\omega_0 t'} + c.c.$, with *c.c.* denoting the complex conjugate part. At the second order
 329 in ϵ , the imposition of a solvability condition necessary to avoid secular terms prescribes the
 330 amplitude $B(T) = A(T) e^{-i\lambda T/2}$ to obey the following amplitude equation

$$331 \quad \frac{dB}{dT} = -\frac{\sigma_0}{2}B - i\frac{\lambda}{2}B - i\frac{\omega_0}{4(1+\Gamma)}f\bar{B}. \quad (2.33)$$

332 Turning to polar coordinates, i.e. $B = |B|e^{i\Phi}$, keeping in mind that $\sigma_0 = \sigma_{0,r} + i\sigma_{0,i}$ and
 333 looking for stationary solutions with $|B| \neq 0$ (we skip the straightforward mathematical
 334 steps), one ends up with the following approximation for the marginal stability boundaries
 335 associated with the first sub-harmonic Faraday tongue

$$336 \quad \left(\frac{\Omega + \sigma_{0,i}}{2\omega_0} - 1 \right) = \pm \frac{1}{4(1+\Gamma)} \sqrt{f^2 - \frac{4\sigma_{0,r}^2(1+\Gamma)^2}{\omega_0^2}}, \quad (2.34)$$

337 whose onset acceleration value, $\min f_{SH1}$, for a fixed driving frequency $\Omega/2\pi$, amounts to

$$338 \quad \min f_{SH1} = 2\sigma_{0,r} \sqrt{\frac{1+\Gamma}{gk \tanh kh}} \approx 2\sigma_{0,r} \sqrt{\frac{1}{g} \left(\frac{1}{k} + \frac{\gamma}{\rho g} k \right)}, \quad (2.35)$$

339 Note that the final approximation on the right-hand-side of (2.35) only holds if $kh \gg 1$, so that
 340 $\tanh kh \approx 1$ (deep water regime). Given that $\chi_{0,r} > 12$ and $\chi_{0,i} > 0$ always, the asymptotic
 341 approximation (2.35), in its range of validity, suggests that Darcy's model underestimates
 342 the sub-harmonic stability threshold. Moreover, from (2.34), the critical wavenumber k ,
 343 associated with $\min f_{SH1}$, would correspond to that prescribed by the Darcy approximation
 344 but at an effective forcing frequency $\Omega + \sigma_{0,i} = 2\omega_0$ instead of at $\Omega = 2\omega_0$. This explains
 345 why the modified tongues appear shifted towards higher wavenumbers. These observations
 346 are well visible in figure 4.

347 2.2.2. First harmonic tongue

348 By analogy with §2.2.1, an analytical approximation of the first harmonic tongue (H1) can
 349 be provided. In the same spirit of Rajchenbach & Clamond (2015), we adapt the asymptotic

| Liquid | μ [mPa s] | ρ [kg/m ³] | γ [N/m] | M [Pa s] |
|---------------|---------------|-----------------------------|----------------|------------|
| ethanol 99.7% | 1.096 | 785 | 0.0218 | 0.04 |
| ethanol 70.0% | 2.159 | 835 | 0.0234 | 0.0485 |
| ethanol 50.0% | 2.362 | 926 | 0.0296 | 0.07 |

Table 1: Characteristic fluid parameters for the three ethanol-water mixtures considered in this study. Data for the pure ethanol and ethanol-water mixture (50%) are taken from Li *et al.* (2019). The value of the friction parameter M for ethanol-70% is fitted from the experimental measurements reported in §4, but lies well within the range of values used by Li *et al.* (2019) and agrees with the linear trend displayed in figure 5 of Hamraoui *et al.* (2000).

350 scaling such that f is still of order ϵ , but $T = \epsilon^2$, $\hat{\sigma}_n = \sigma_1 \sim \epsilon^2$ (with $\xi_1 \Omega = \Omega$) and
 351 $\Omega = \omega_0 + \epsilon^2 \lambda$. Pursuing the expansion up to ϵ^2 -order, with $\hat{\eta}_0 = A(T) e^{i\omega_0 t'} + c.c.$ and
 352 $B(T) = A(T) e^{-i\lambda T}$, will provide the amplitude equation

$$353 \quad \frac{dB}{dT} = -\frac{\sigma_1}{2} B - i\lambda B - i\frac{\omega_0}{8(1+\Gamma)^2} f^2 \bar{B} + i\frac{\omega_0}{12(1+\Gamma)^2} f^2 B. \quad (2.36)$$

354 The approximation for the marginal stability boundaries derived from (2.36) takes the form

$$355 \quad \left(\frac{\Omega + \sigma_{1,i}/2}{\omega_0} - 1 \right) = \frac{f^2}{12(1+\Gamma)^2} \pm \frac{1}{8(1+\Gamma)^2} \sqrt{f^4 - \left(\frac{4\sigma_{1,r}(1+\Gamma)^2}{\omega_0} \right)^2} \quad (2.37)$$

356 with a minimum onset acceleration, $\min f_{1H}$

$$357 \quad \min f_H = 2\sqrt{\sigma_{1,r}} \left(\frac{(1+\Gamma)^3}{gk \tanh kh} \right)^{1/4} \approx 2\sqrt{\sigma_{1,r}} \frac{1}{g^{1/4}} \left(\frac{1}{k^{1/3}} + \frac{\gamma}{\rho g} k^{5/3} \right)^{3/4}, \quad (2.38)$$

358 and where, as before, the final approximation on the right-hand side is only valid in the deep
 359 water regime. Similarly to the sub-harmonic case, the critical wavenumber k corresponds to
 360 that prescribed by the Darcy approximation but at an effective forcing frequency $\Omega + \sigma_{1,i}/2 =$
 361 ω_0 instead of at $\Omega = \omega_0$ and the onset acceleration is larger than that predicted from the
 362 Darcy approximation (as $\chi_{1,r} > 12$).

363 2.3. Comparison with experiments by Li et al. (2019)

364 Results presented so far were produced by assuming the absence of contact line dissipation,
 365 i.e. coefficient M was set to $M = 0$, so that $\sigma_{CL} = 0$. In this section, we reintroduce
 366 such a dissipative contribution and we compare our theoretical predictions with a set of
 367 experimental measurements reported by Li *et al.* (2019), using the values they have proposed
 368 for M . This comparison, shown in figure 5, is outlined in terms of non-dimensional minimum
 369 onset acceleration, $\min f = \min f_{SH1}$, versus driving frequency. These authors performed
 370 experiments in two different Hele-Shaw cells of length $l = 300$ mm, fluid depth $h = 60$ mm
 371 and gap-size $b = 2$ mm or $b = 5$ mm. Two fluids, whose properties are reported in table 1, were
 372 used: ethanol 99.7% and ethanol 50%. The empty squares in figure 5 are computed via Floquet
 373 stability analysis (2.31) using the Darcy approximation for $\sigma_{BL} = 12\nu/b^2$ and correspond to
 374 the theoretical prediction by Li *et al.* (2019), while the colored triangles are computed using
 375 the present theory, with the corrected $\sigma_{BL} = \chi_n \nu/b^2$. Although the trend is approximately
 376 the same, the Darcy approximation underestimates the onset acceleration with respect to the

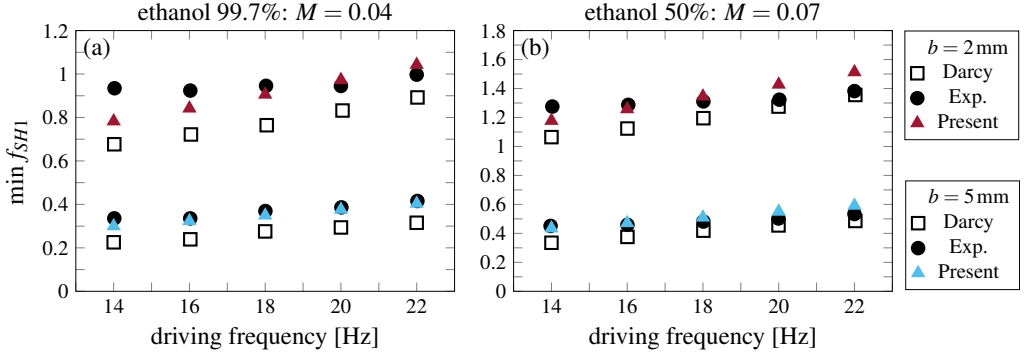


Figure 5: Sub-harmonic instability onset, $\min f$, versus driving frequency, $\Omega/2\pi$.

Comparison between theoretical data (empty squares: standard Darcy model, $\sigma_{BL} = 12\nu/b^2$; colored triangles: present model, $\sigma_{BL} = \chi_n\nu/b^2$) and experimental measurements by Li *et al.* (2019). The values of the mobility parameter M here employed are reported in the figure.

present model, which overall compares better with the experimental measurements (black-filled circles). Some disagreement still exists, especially at smaller cell gaps, i.e. $b = 2$ mm, where surface tension effects are even larger. This is likely attributable to an imperfect phenomenological contact line model (Bongarzone *et al.* 2021, 2022), whose definition falls beyond the scope of this work. Yet, this comparison shows how the modifications introduced by the present model contribute to closing the gap between theoretical Faraday onset estimates and these experiments.

3. The case of thin annuli

We now consider the case of a thin annular container, whose nominal radius is R and the actual inner and outer radii are $R - b/2$ and $R + b/2$, respectively (see the sketch in figure 1(b)). In the limit of $b/R \ll 1$, the wall curvature is negligible and the annular container can be considered a Hele-Shaw cell. The following change of variable for the radial coordinate, $r' = R + y' = R(1 + y'/R)$ with $y' \in [-b/2, b/2]$, will be useful in the rest of the analysis. As in §2, we first linearize around the rest state. Successively, we introduce the following non-dimensional quantities,

$$r = \frac{r'}{R}, \quad y = \frac{y'}{b}, \quad z = \frac{z'}{R}, \quad u = \frac{u'_\varphi}{a\Omega}, \quad v = \frac{u'_r}{a\Omega(b/R)}, \quad w = \frac{u'_z}{a\Omega}, \quad p = \frac{p'}{\rho Ra\Omega^2}. \quad (3.1)$$

It follows that, at leading order, $r = 1 + yb/R \sim 1 \longrightarrow 1/r = 1/(1 + yb/R) \sim 1$ but $\partial/\partial_r = (R/b)\partial/\partial_y \sim (b/R)^{-1} \gg 1$. With this scaling and introducing the Floquet ansatz (2.6a)-(2.6b), one obtains the following simplified governing equations,

$$\frac{\partial \tilde{u}_n}{\partial \varphi} + \frac{\partial \tilde{v}_n}{\partial y} + \frac{\partial \tilde{w}_n}{\partial z} = 0, \quad (3.2a)$$

$$i\tilde{u}_n = -\frac{1}{\xi_n} \frac{\partial \tilde{p}_n}{\partial \varphi} + \frac{\delta_n^2}{2} \frac{\partial^2 \tilde{u}_n}{\partial y^2}, \quad i\tilde{w}_n = -\frac{1}{\xi_n} \frac{\partial \tilde{p}_n}{\partial z} + \frac{\delta_n^2}{2} \frac{\partial^2 \tilde{w}_n}{\partial y^2} \quad \text{or} \quad \tilde{\mathbf{u}}_n = \frac{i}{\xi_n} \nabla \tilde{p}_n F_n(y), \quad (3.2b)$$

which are fully equivalent to those for the case of conventional rectangular cells if the transformation $\varphi \rightarrow x$ is introduced. Averaging the continuity equation with the imposition

401 of the no-penetration condition at $y = \mp 1/2$, $v(\mp 1/2)$, eventually leads to

402

$$\nabla^2 \tilde{p}_n = \frac{\partial^2 \tilde{p}_n}{\partial z^2} + \frac{\partial^2 \tilde{p}_n}{\partial \varphi^2}, \quad (3.3)$$

403 identically to (2.11). Expanding \tilde{p}_n in the azimuthal direction as $\tilde{p}_n = \hat{p}_n \sin m\varphi$, with m the
404 azimuthal wavenumber, provides

405

$$\left(\frac{\partial^2}{\partial z^2} - m^2 \right) \hat{p}_n = 0 \quad \longrightarrow \quad \hat{p}_n = c_1 \cosh mz + c_2 \sinh mz, \quad (3.4)$$

406 and the no-penetration condition at the solid bottom located at $z = -h/R$, $\hat{w}_n = \partial_z \hat{p}_n = 0$,
407 prescribes

408

$$\hat{p}_n = c_1 (\cosh mz + \tanh mh/R \sinh mz). \quad (3.5)$$

409 Although so far the theory for the rectangular and the annular cases is basically the same, here
410 it is crucial to observe that the axisymmetric container geometry translates into a periodicity
411 condition:

412

$$\sin(-m\pi) = \sin(m\pi) \quad \longrightarrow \quad \sin m\pi = 0, \quad (3.6)$$

413 which always imposes the azimuthal wavenumber to be an integer. In other words, in
414 contradistinction with the case of §2, where the absence of lateral wall ideally allows for any
415 wavenumber k , here we have $m = 0, 1, 2, 3, \dots \in \mathbb{N}$.

416 By repeating the calculations outlined in §2, one ends up with the same equation (2.28)
417 (and subsequent (2.29)-(2.31)), but where ω_0 obeys to the *quantized* dispersion relation

418

$$\omega_0^2 = \left(\frac{g}{R} m + \frac{\gamma}{\rho R^3} m^3 \right) \tanh m \frac{h}{R} = (1 + \Gamma) \frac{g}{R} m \tanh m \frac{h}{R}. \quad (3.7)$$

419 with $\Gamma = \gamma m^2 / \rho g R^2$. In this context, a representation of Faraday's tongues in the forcing
420 frequency-amplitude plane appears most natural, as each parametric tongue will correspond
421 to a fixed wavenumber m . Consequently, instead of fixing Ω and varying the wavenumber,
422 here we solve (2.31) by fixing m and varying Ω .

423 3.1. Floquet analysis and asymptotic approximation

424 The results from this procedure are reported in figure 6, where, as in figure 3, the black
425 regions correspond to the unstable tongues obtained according to the standard gap-averaged
426 Darcy model, while the red ones are computed using the present theory with the corrected
427 gap-averaged $\sigma_{BL} = \chi_n v/b^2$. The Faraday threshold is represented in terms of forcing
428 acceleration (panels (a) and (b)) and forcing amplitude (panels (c) and (d)). Note the prediction
429 reported in panels (c) and (d) are equivalent to those reported in panels (a) and (b) with the
430 ordinate rescaled by a factor Ω^2/g . In figure 6(a)-(c) no contact line model is included,
431 whereas in (b)-(d) a mobility parameter $M = 0.0485$ is accounted for. The use of this specific
432 value for M will be clarified in the next section when comparing the theory with dedicated
433 experiments. The regions with the lowest thresholds in each panel are sub-harmonic tongues
434 associated with modes from $m = 1$ to 14.

435 In general, the present model gives a higher instability threshold, consistent with the results
436 reported in the previous section. However, the tongues are here shifted to the left.

437 The asymptotic approximation for the sub-harmonic onset acceleration, adapted to this
438 case from (2.34) yields:

439

$$f_{SH1} = 2 \sqrt{(1 + \Gamma) \frac{\sigma_{0,r}^2}{(g/R) m \tanh mh/R} + 4(1 + \Gamma)^2 \left(\frac{\Omega + \sigma_{0,i}}{2\omega_0} - 1 \right)^2}, \quad (3.8)$$

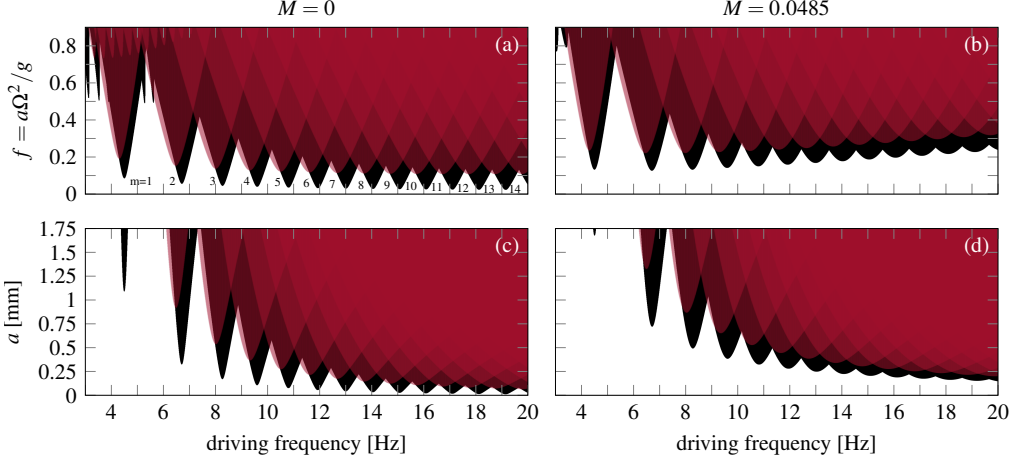


Figure 6: Faraday tongues computed via Floquet analysis (2.31) at different fixed azimuthal wavenumber m and varying the driving frequency, $\Omega/2/\pi$. (a)-(b) Faraday thresholds in terms of forcing acceleration $f = a\Omega^2/g$; (c)-(d) Threshold in terms of forcing amplitude a . Black regions correspond to the unstable Faraday tongues computed using $\sigma_{BL} = 12\nu/b^2$, whereas red regions are the unstable tongues computed with the present modified $\sigma_{BL} = \chi_n\nu/b^2$. The fluid parameters used here correspond to those given in table 1 for ethanol 70%. The gap-size is set to $b = 7$ mm, the fluid depth to $h = 65$ mm and the nominal radius to $R = 44$ mm. Contact line dissipation is included in (b) and (d) by accounting for a mobility coefficient $M = 0.0485$. The regions with the lowest thresholds in each panel are sub-harmonic tongues associated with modes from $m = 1$ to 14.

440 with

$$441 \quad \min f_{SH1} = 2\sigma_{0,r} \frac{1 + \Gamma}{\omega_0} = 2\sigma_{0,r} \sqrt{\frac{1 + \Gamma}{(g/R)m \tanh mh/R}} \approx 2\sigma_{0,r} \sqrt{\frac{R}{g} \left(\frac{1}{m} + \frac{\gamma}{\rho g R^2} m \right)}, \quad (3.9)$$

442 helps us indeed in rationalizing the influence of the modified complex damping coefficient.
443 This apparent opposite correction is a natural consequence of the different representations:
444 varying wavenumber at a fixed forcing frequency (as in figure 3) versus varying forcing
445 frequency at a fixed wavenumber (figure 6). Such a behaviour is clarified by the asymptotic
446 relation (3.8) and, particularly by the term $\left(\frac{\Omega + \sigma_{0,i}}{2\omega_0} - 1\right)$. In §2, the analysis is based on a
447 fixed forcing frequency, while the wavenumber k and, hence, the natural frequency ω_0 , are
448 let free to vary. The first sub-harmonic Faraday tongue occurs when $\Omega + \sigma_{0,i} \approx 2\omega_0$. Since
449 Ω is fixed and $\sigma_{0,i} > 0$, $\Omega + \sigma_{0,i} > \Omega$ such that ω_0 and therefore k have to increase in
450 order to satisfy the relation. On the other hand, if the wavenumber m and, hence, ω_0 are
451 fixed as in this section, then $2\omega_0 - \sigma_{0,i} < 2\omega_0$ and the forcing frequency around which the
452 sub-harmonic resonance is centered, decreases of a contribution $\sigma_{0,i}$, which introduces a
453 frequency detuning responsible for the negative frequency shift displayed in figure 6.

454

455 3.2. Discussion on the system's spatial quantization

456 A first aspect that needs to be better discussed is the frequency-dependence of the damping
457 coefficient σ_n associated with each Faraday's tongue. In the case of horizontally infinite
458 cells, the most natural description for investigating the system's stability properties is in the
459 (k, f) plane for a fixed forcing angular frequency Ω (Kumar & Tuckerman 1994). According

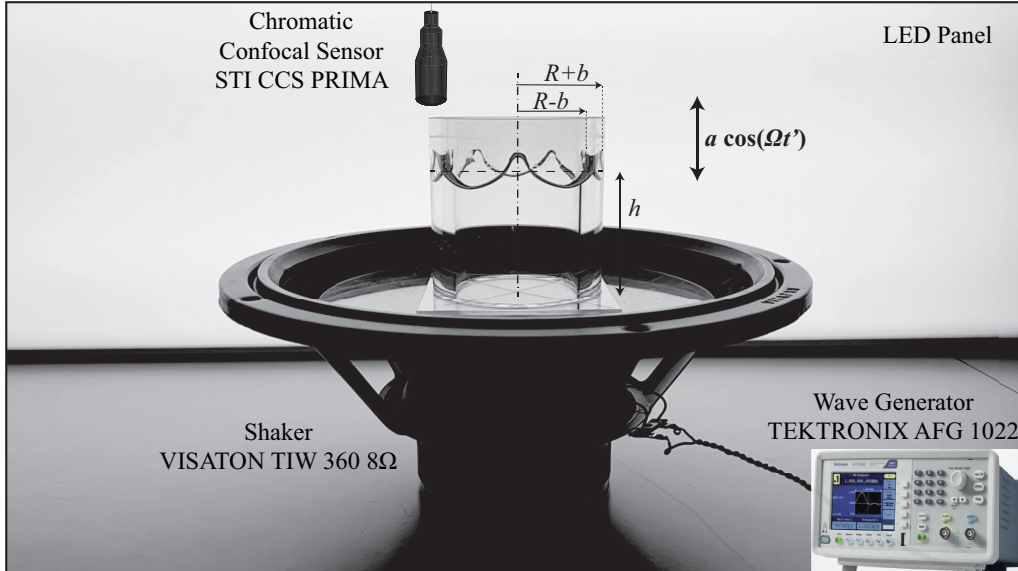


Figure 7: Photo of the experimental setup

460 to our model, the oscillating system's response occurring within each tongue is characterized
 461 by a Stokes boundary layer thickness $\delta_n = \sqrt{2\nu/(n\Omega + \alpha)}/b$. For instance, let us consider
 462 sub-harmonic resonances with $\alpha = \Omega/2$. As Ω is fixed (see any sub-panel of figure 3), each
 463 unstable region sees a constant δ_n (with $n = 0, 1, 2, \dots$) and hence a constant damping σ_n .

464 On the other hand, in the case of quantized wavenumber as for the annular cell of §3,
 465 the most suitable description is in the driving frequency-driving amplitude plane at fixed
 466 wavenumber m (see figure 6) (Batson *et al.* 2013). In this description, each sub-harmonic
 467 ($\alpha = \Omega/2$) or harmonic ($\alpha = \Omega$) n th tongue associated with a wavenumber m , sees a δ_n , and
 468 thus a σ_n , changing with Ω along the tongue itself.
 469

470 4. Experiments

471 In a real lab-scale experiment, the horizontal size of rectangular cells is never actually infinite
 472 due to the presence of lateral walls in the elongated direction. In such a case however, the
 473 solution form (2.9) prevents the no-slip condition for the in-plane xz -velocity components
 474 to be imposed (Viola *et al.* 2017). This always translates into a theoretical underestimation
 475 of the overall damping of the system in rectangular Hele-Shaw cells, although the sidewall
 476 contribution is expected to be negligible for sufficiently long cells.

477 On the other hand, the case of a thin annulus, by naturally filtering out this extra dissipation
 478 owing to the periodicity condition, offers a prototype configuration that can potentially allow
 479 one to better quantify the correction introduced by the present gap-averaged model when
 480 compared to dedicated experiments.

481 4.1. Setup

482 The experimental apparatus, shown in figure 7, consists in a Plexiglas annular container of
 483 height 100 mm, nominal radius $R = 44$ mm and gap-size $b = 7$ mm, which is then filled to a
 484 depth $h = 65$ mm with ethanol 70% (see table 1 for the fluid properties). An air conditioning
 485 system helps in maintaining the temperature of the room at around 22°. The container is

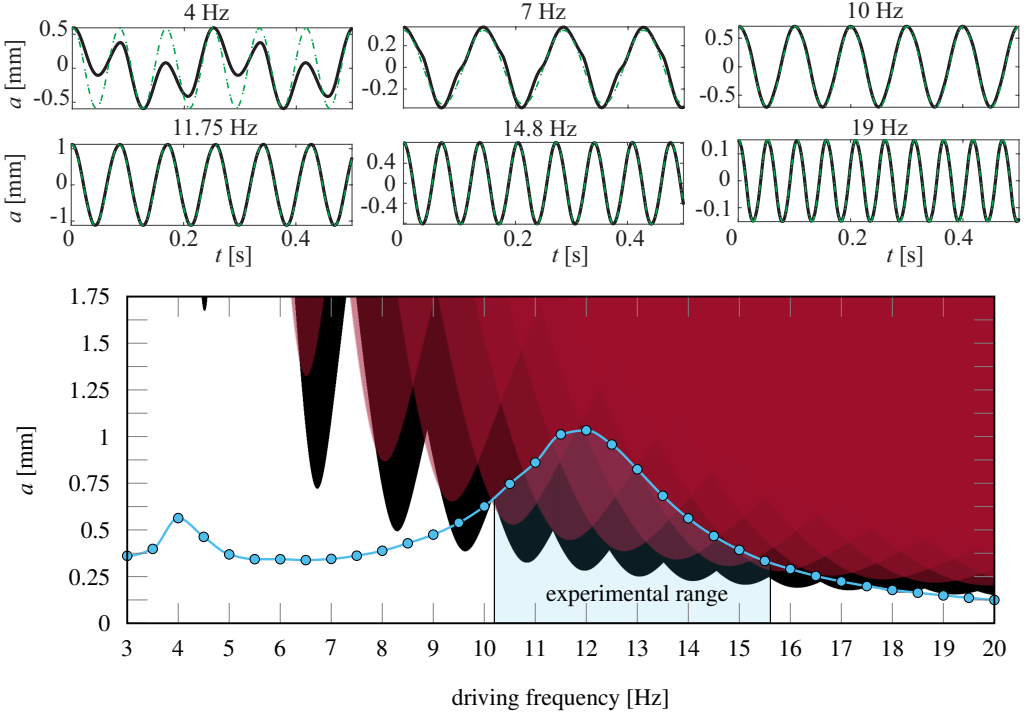


Figure 8: *Top*: vertical container displacement a versus time at different forcing frequencies. The black curves are the measured signal, while the green dash-dotted curves are sinusoidal fitting. Below a forcing frequency of 8 Hz, the loudspeaker's output begins to depart from a sinusoidal signal. *Bottom*: same as in figure 6(d): sub-harmonic Faraday tongues computed by accounting for contact line dissipation with a mobility parameter $M = 0.0485$. The light blue curve here superposed corresponds to the maximal vertical displacement a achievable with our setup. With this constraint, Faraday waves are expected to be observable only in the frequency range highlighted in blue.

486 mounted on a loudspeaker VISCATON TIW 360 8Ω placed on a flat table and connected
 487 to a wave generator TEKTRONIX AFG 1022, whose output signal is amplified using a
 488 wideband amplifier THURKBY THUNDER WA301. The motion of the free surface is
 489 recorded with a digital camera NIKON D850 coupled with a 60mm f/2.8D lens and operated
 490 in slow motion mode, allowing for an acquisition frequency of 120 frames per second. A
 491 LED panel placed behind the apparatus provides back illumination of the fluid interface
 492 for better optimal contrast. The wave generator imposes a sinusoidal alternating voltage,
 493 $v = (V_{pp}/2) \cos(\Omega t')$, with Ω the angular frequency and V_{pp} the full peak-to-peak voltage.
 494 The response of the loudspeaker to this input translates into a vertical harmonic motion of
 495 the container, $a \cos(\Omega t')$, whose amplitude, a [mm], is measured with a chromatic confocal
 496 displacement sensor STI CCS PRIMA/CLS-MG20. This optical pen, which is placed around
 497 2 cm (within the admissible working range of 2.5 cm) above the container and points at the
 498 top flat surface of the outer container's wall, can detect the time-varying distance between the
 499 fixed sensor and the oscillating container's surface with a sampling rate in the order of kHz
 500 and a precision of $\pm 1 \mu\text{m}$. Therefore, the pen can be used to obtain a very precise real-time
 501 value of a as the voltage amplitude V_{pp} and the frequency Ω are adjusted.

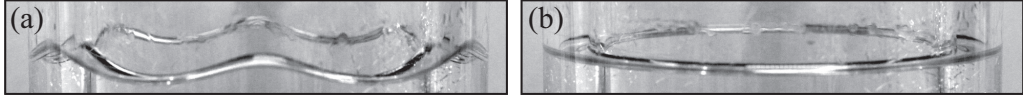


Figure 9: Free surface shape at a forcing frequency $1/T = 11.7$ Hz and corresponding to: (a) the lowest forcing amplitude value, $a = 0.4693$ mm, for which the $m = 6$ standing wave is present (the figure shows a temporal snapshot); (b) the largest forcing amplitude value, $a = 0.4158$ mm, for which the surface becomes flat and stable again. Despite the small forcing amplitude variation, the change in amplitude is large enough to allow for a visual inspection of the instability threshold with sufficient accuracy.

502 4.2. Identification of the accessible experimental range

503 Such a simple setup, however, put some constraints on the explorable experimental frequency
504 range.

505 (i) First, we need to ensure that the loudspeaker's output translates into a vertical container's
506 displacement following a sinusoidal time signal. To this end, the optical sensor is used to
507 measure the container motion at different driving frequencies. These time signals are then
508 fitted with a sinusoidal law. Figure 8 shows how below a forcing frequency of 8 Hz, the
509 loudspeaker's output begins to depart from a sinusoidal signal. This check imposes a first
510 lower bound on the explorable frequency range.

511 (ii) In addition, as Faraday waves only appear above a threshold amplitude, it is convenient
512 to measure *a priori* the maximal vertical displacement a achievable. The loudspeaker
513 response curve is reported in the bottom part of figure 8. A superposition of this curve with
514 the predicted Faraday's tongues immediately identifies the experimental frequency range
515 within which the maximal achievable a is larger than the predicted Faraday threshold so that
516 standing waves are expected to emerge in our experiments. Assuming the herein proposed
517 gap-averaged model (red regions) to give a good prediction of the actual instability onset,
518 the experimental range explored in the next section is limited to approximately $\in [10.2, 15.6]$
519 Hz.

520 4.3. Procedure

521 Given the constraints discussed in §4.2, experiments have been carried out in a frequency
522 range between 10.2 Hz and 15.6 Hz with a frequency step of 0.1 Hz. For each fixed forcing
523 frequency, the Faraday threshold is determined as follows: the forcing amplitude a is set to
524 the maximal value achievable by the loudspeaker, so as to quickly trigger the emergence of
525 the unstable Faraday wave. The amplitude is then progressively decreased until the wave
526 disappears and the surface becomes flat again.

527 More precisely, a first quick pass across the threshold is made to determine an estimate
528 of the sought amplitude. A second pass is then made by starting again from the maximum
529 amplitude and decreasing it. When we approach the value determined during the first pass,
530 we perform finer amplitude decrements, and we wait several minutes between each amplitude
531 change to ensure that the wave stably persists. We eventually identify two values: the last
532 amplitude where the instabilities were present (see figure 9(a)) and the first one where the
533 surface becomes flat again (see figure 9(b)). Two more runs following an identical procedure
534 are then performed to verify the values previously found. Lastly, an average between the
535 smallest unstable amplitude and the largest stable one gives us the desired threshold.

536 Once the threshold amplitude value is found for the considered frequency, the output of the
537 wave generator is switched off, the frequency is changed, and the steps presented above are
538 repeated again for the new frequency. In this way we always start from a stable configuration,
539 hence limiting the possibility of nonlinear interaction between different modes.

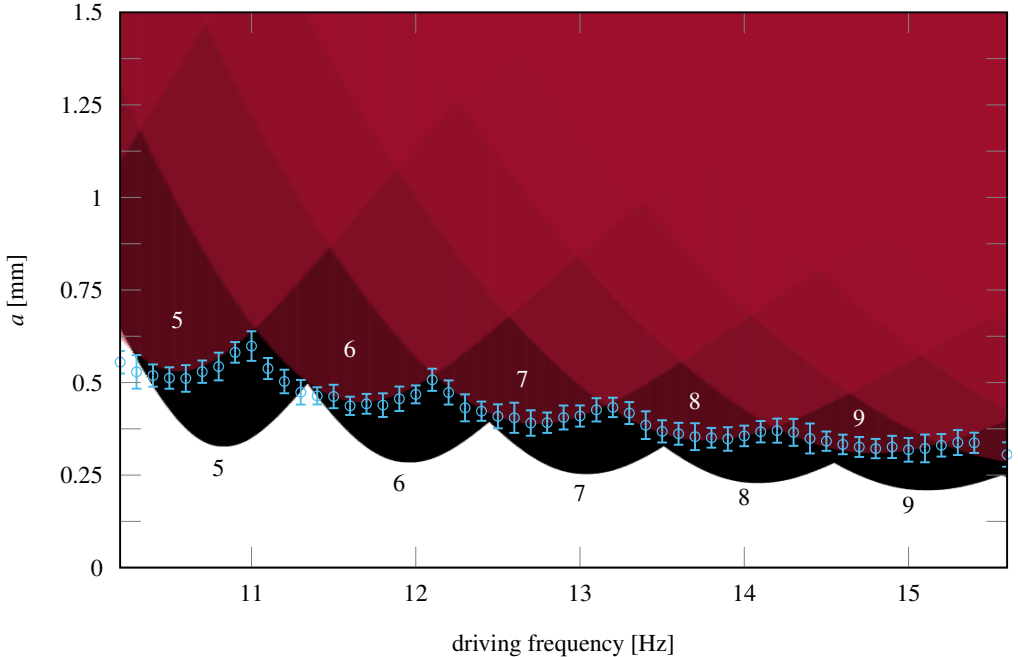


Figure 10: Experiments (empty circles) are compared to the theoretically predicted sub-harmonic Faraday threshold computed via Floquet analysis (2.31) for different fixed azimuthal wavenumber m and according to the standard (black region) and revised (red regions) gap-averaged models. The shaded band around the instability onset indicates the error bar for the threshold amplitudes at each measured driving frequency. The tongues are computed by including contact line dissipation with a value of M equal to 0.0485 as in figures 6(b)-(d) and 8. As explained in §4.3, the vertical error bars indicate the amplitude range between the smallest measured forcing amplitude at which the instability was detected and the largest one at which the surface remains stable and flat. These two limiting values are successively corrected by accounting for the optical pen's measurement error and the non-uniformity of the output signal of the loudspeaker.

540 For each forcing frequency, the two limiting amplitude values, identified as described
 541 above, are used to define the error bars reported in figure 10. Those error bars must also
 542 account for the optical pen's measurement error ($0.1 \mu\text{m}$), as well as the non-uniformity of
 543 the output signal. By looking at the measured average, minimum, and maximum amplitude
 544 values in the temporal output signal, it is noteworthy that the average value typically deviates
 545 from the minimum and maximum by around $10 \mu\text{m}$. Consequently, we incorporate in the
 546 error bars this additional $10 \mu\text{m}$ of uncertainty in the value of a . The uncertainty in the
 547 frequency of the output signal is not included in the definition of the error bars, as it is
 548 extremely small, on the order of 0.001 Hz.
 549

550 4.4. Instability onset and wave patterns

551 The experimentally detected threshold at each measured frequency is reported in figure 10
 552 in terms of forcing acceleration f and amplitude a . Once again, the black unstable regions
 553 are calculated according to the standard gap-averaged model with $\sigma_{BL} = 12\nu/b^2$, whereas
 554 red regions are the unstable tongues computed using the modified damping $\sigma_{BL} = \chi_n\nu/b^2$.
 555 Both scenarios include contact line dissipation $\sigma_{CL} = (2M/\rho b)(m/R)\tanh(mh/R)$, with a

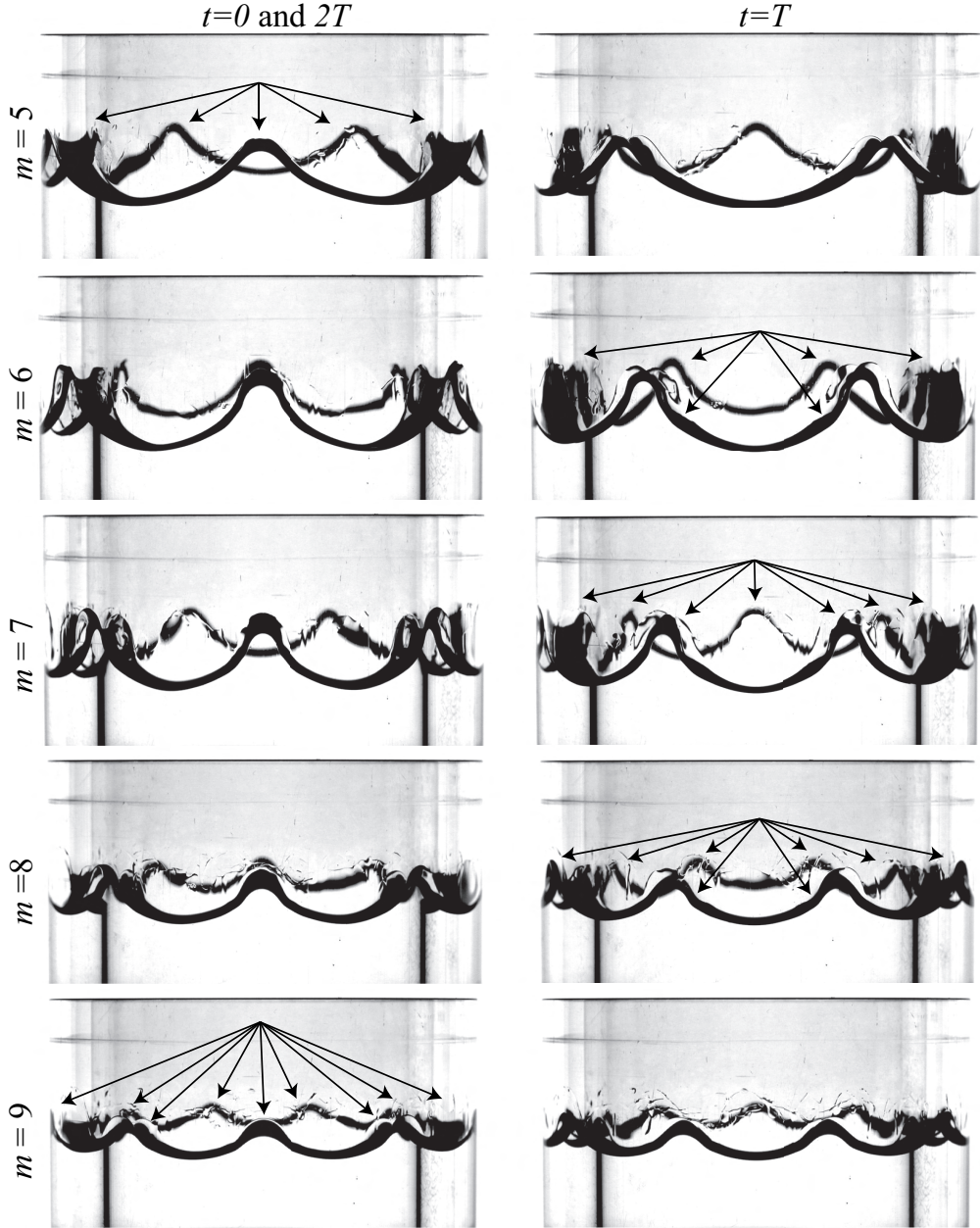


Figure 11: Snapshots of the wave patterns experimentally observed within the sub-harmonic Faraday tongues associated with the azimuthal wavenumbers $m = 5, 6, 7, 8$ and 9 . T is the forcing period, which is approximately half the oscillation period of the wave response. These patterns appear for: $(m = 5) 1/T = 10.6 \text{ Hz}, a = 0.8 \text{ mm}$; $(m = 6) 1/T = 11.6 \text{ Hz}, a = 1.1 \text{ mm}$; $(m = 7) 1/T = 12.7 \text{ Hz}, a = 0.9 \text{ mm}$; $(m = 8) 1/T = 13.7 \text{ Hz}, a = 0.6 \text{ mm}$; $(m = 9) 1/T = 14.8 \text{ Hz}, a = 0.4 \text{ mm}$. These forcing amplitudes are the maximal achievable at their corresponding frequencies (see figure 8 for the associated operating points). The number of peaks is easily countable by visual inspection of two time snapshots of the oscillating pattern exacted at $t = 0, T$ and $t = T/2$. This provides a simple criterion for the identification of the resonant wavenumber m . See also supplementary movies 1-5 at: [LINK](#).

556 value of M equal to 0.0485 for ethanol 70%. Although, at first, this value has been simply
 557 selected in order to fit well our experimental measurements, it is in perfect agreement with
 558 the linear relation linking M to the liquid's surface tension reported in figure 5 of Hamraoui
 559 *et al.* (2000) and used by Li *et al.* (2019) (see table 1).

560 As figure 10 strikingly shows, the present theoretical thresholds match well our experimen-
 561 tical measurements. On the contrary, the poor description of the oscillating boundary layer
 562 in the classical Darcy model translates into a lack of viscous dissipation. The arbitrary choice
 563 of a higher fitting parameter M value, e.g. $M \approx 0.09$ would increase contact line dissipation
 564 and compensate for the underestimated Stokes boundary layer one, hence bringing these
 565 predictions much closer to experiments; however, such a value would lie well beyond
 566 the typical values reported in the literature. Furthermore, the real damping coefficient
 567 $\sigma_{BL} = 12\nu/b^2$ given by the Darcy theory does not account for the frequency detuning
 568 displayed by experiments. This frequency shift is instead well captured by the imaginary part
 569 of the new damping $\sigma_{BL} = \chi_n\nu/b^2$ (with $\chi_n = \chi_{n,r} + i\chi_{n,i}$).

570 Within the experimental frequency range considered, five different standing waves,
 571 corresponding to $m = 5, 6, 7, 8$ and 9, have emerged. The identification of the wavenumber
 572 m has been simply performed by visual inspection of the free surface patterns reported in
 573 figure 11. Indeed, by looking at a time snapshot, it is possible to count the various wave
 574 peaks along the azimuthal direction.

575 When looking at figure 10, it is worth commenting that on the left sides of the marginal
 576 stability boundaries associated with modes $m = 5$ and 6 we still have a little discrepancy
 577 between experiments and the model. Particularly, the experimental thresholds are slightly
 578 lower than the predicted ones. A possible explanation can be given by noticing that our
 579 experimental protocol is agnostic to the possibility of subcritical bifurcations and hysteresis,
 580 while such behaviour has been predicted by Douady (1990).

581 As a last comment, one has to keep in mind that the Hele-Shaw approximation remains
 582 good only if the wavelength, $2\pi R/m$ does not become too small, i.e. comparable to the cell's
 583 gap, b . In other words, one must check that the ratio $mb/2\pi R$ is of the order of the small
 584 separation-of-scale parameter, ϵ . For the largest wavenumber observed in our experiments,
 585 $m = 9$, the ratio $mb/2\pi R$ amounts to 0.23, which is not exactly small. Yet, the Hele-Shaw
 586 approximation is seen to remain fairly good.

587 4.5. Contact angle variation and thin film deposition

588 Before concluding, it is worth commenting on why the use of dynamic contact angle
 589 model (2.21) is justifiable and seen to give good estimates of the Faraday thresholds.

590 Existing lab experiments have revealed that liquid oscillations in Hele-Shaw cells con-
 591 stantly experience an up-and-down driving force with an apparent contact angle θ constantly
 592 changing (Jiang *et al.* 2004). Our experiments are consistent with such evidence. In figure 12
 593 we report seven snapshots, (i)-(vii), covering one oscillation period, T , for the container
 594 motion. These snapshots illustrate a zoom of the dynamic meniscus profile and show how
 595 the macroscopic contact angle changes in time during the second half of the advancing cycle
 596 (i)-(v) and the first half of the receding cycle (vi)-(x), hence highlighting the importance
 597 of the out-of-plane meniscus curvature variations. Thus, on the basis of our observations,
 598 it seemed appropriate to introduce in the theory a contact angle model so as to justify this
 599 associated additional dissipation, which would be neglected by assuming $M = 0$. The model
 600 used in this study, and already implemented by Li *et al.* (2019), is very simple; it assumes the
 601 cosine of the dynamic contact angle to linearly depend on the contact line speed through the
 602 capillary number Ca (Hamraoui *et al.* 2000). Accounting for such a model is shown, both
 603 in Li *et al.* (2019) and in this study, to supplement the theoretical predictions by a sufficient
 604 extra dissipation suitable to match experimental measurements.

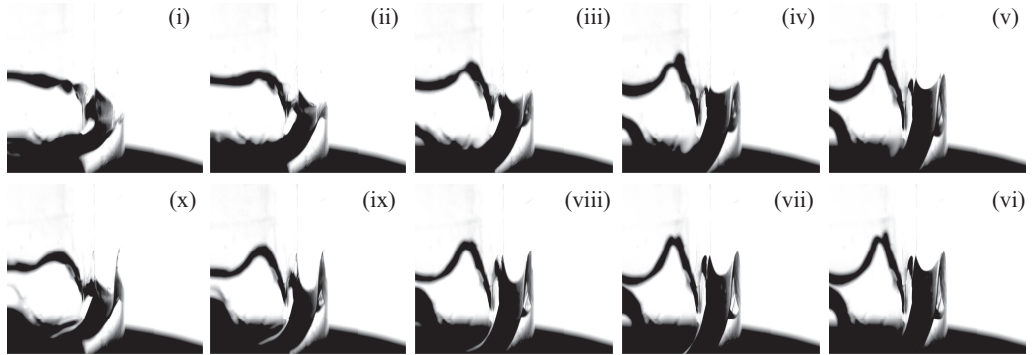


Figure 12: Zoom of the meniscus dynamics recorded at a driving frequency 11.6 Hz and amplitude $a = 1.2$ mm for $m = 6$. Seven snapshots, (i)-(vii), covering one oscillation period, T , for the container motion are illustrated. These snapshots show how the meniscus profile and the macroscopic contact angle change in time during the second half of the advancing cycle and the first half of the receding cycle, hence highlighting the importance of the out-of-plane curvature or capillary effects. See also supplementary movie 6 at: [LINK](#).

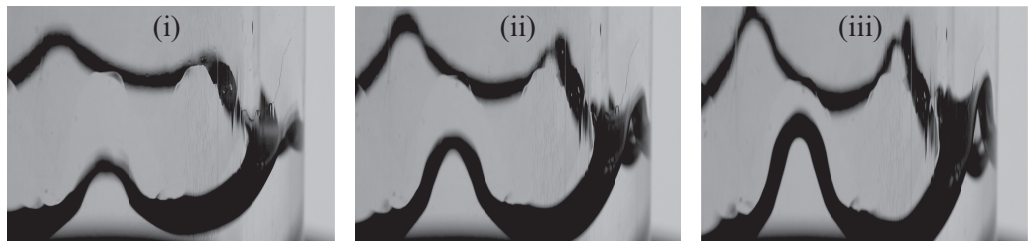


Figure 13: These three snapshots correspond to snapshots (ii), (iii) and (iv) of figure 12 and show, using a different light contrast, how the contact line constantly moves over a wetted substrate due to the presence of a stable thin film deposited and alimented at each cycle.

605 This dissipation eventually reduces to a simple damping coefficient σ_{CL} as it is of
 606 linear nature. A unique constant value of the mobility parameter M is sufficient to fit all
 607 our experimental measurements at once, suggesting that the meniscus dynamics is not
 608 significantly affected by the evolution of the wave in the azimuthal direction, i.e. by the
 609 wavenumber, and M can be seen as an intrinsic property of the liquid-substrate interface.
 610

611 Several studies have discussed the dependence of the system's dissipation on the substrate
 612 material (Huh & Scriven 1971; Dussan 1979; Coccia *et al.* 1993; Ting & Perlin 1995; Eral
 613 *et al.* 2013; Viola *et al.* 2018; Viola & Gallaire 2018; Xia & Steen 2018). These authors,
 614 among others, have unveiled and rationalized interesting features such as solid-like friction
 615 induced by contact angle hysteresis. This strongly nonlinear contact line behaviour does
 616 not seem to be present in our experiments. This can be tentatively explained by looking
 617 at figure 13. These snapshots illustrate how the contact line constantly flows over a wetted
 618 substrate, due to the presence of a stable thin film deposited and alimented at each oscillation
 619 cycle. This feature has been also recently described by Dollet *et al.* (2020), who showed that
 620 the relaxation dynamics of liquid oscillation in a U-shaped tube filled with ethanol, due to the
 621 presence of a similar thin film, obey an exponential law that can be well-fitted by introducing
 a simple linear damping, as done in this work.

622 **5. Conclusions**

623 Previous theoretical analyses for Faraday waves in Hele-Shaw cells have so far relied on the
 624 Darcy approximation, which is based on the parabolic flow profile assumption in the narrow
 625 direction and that translates into a real-valued damping coefficient $\sigma_{BL} = 12\nu/b^2$, with ν the
 626 fluid kinematic viscosity and b the cell's gap-size, that englobes the dissipation originated
 627 from the Stokes boundary layers over the two lateral walls. However, Darcy's model is known
 628 to be inaccurate whenever inertia is not negligible, e.g. in unsteady flows such as oscillating
 629 standing or traveling waves.

630 In this work, we have proposed a gap-averaged linear model that accounts for inertial
 631 effects induced by the unsteady terms in the Navier-Stokes equations, amounting to a pulsatile
 632 flow where the fluid motion reduces to a two-dimensional oscillating flow, reminiscent of
 633 the Womersley flow in cylindrical pipes. When gap-averaging the linearized Navier-Stokes
 634 equation, this results in a modified damping coefficient, $\sigma_{BL} = \chi_n \nu / b^2$, with $\chi_n = \chi_{n,r} + i\chi_{n,i}$
 635 complex-valued, which is a function of the ratio between the Stokes boundary layer thickness
 636 and the cell's gap-size, and whose value depends on the frequency of the system's response
 637 specific to each unstable parametric Faraday tongue.

638 After having revisited the ideal case of infinitely long rectangular Hele-Shaw cells, for
 639 which we have found a good agreement against the experiments by Li *et al.* (2019), we
 640 have considered the case of Faraday waves in thin annuli. This annular geometry, owing
 641 to the periodicity condition, naturally filters out the additional, although small, dissipation
 642 coming from the lateral wall in the elongated direction of finite-size lab-scale Hele-Shaw
 643 cells. Hence, a thin annulus offers a prototype configuration that can allow one to better
 644 quantify the correction introduced by the present gap-averaged theory when compared to
 645 dedicated experiments and to the standard gap-averaged Darcy model.

646 A series of homemade experiments for the latter configuration has proven that Darcy's
 647 model typically underestimates the Faraday threshold, as $\chi_{n,r} > 12$, and overlooks a
 648 frequency detuning introduced by $\chi_{n,i} > 0$, which appears essential to correctly predict
 649 the location of the Faraday's tongue in the frequency spectrum. The frequency-dependent
 650 gap-averaged model here proposed successfully predicts these features and brings the Faraday
 651 thresholds estimated theoretically closer to the ones measured.

652 Furthermore, a close look at the experimentally observed meniscus and contact angle dy-
 653 namics clearly highlighted the importance of the out-of-plane curvature, whose contribution
 654 has been neglected so far in the literature, with the exception of Li *et al.* (2019). This evidence
 655 justifies the employment of a dynamical contact angle model to recover the extra contact line
 656 dissipation and close the gap with experimental measurements.

657 A natural extension of this work is to examine the existence of a drift instability at higher
 658 forcing amplitudes.

659 **Supplementary Material**

660 Supplementary movies 1–5 show the time evolution of the free surface associated with the
 661 snapshots reported in figure 11. Supplementary movie 6 provides instead a better visualization
 662 of the meniscus and the thin film dynamics as illustrated in figures 12 and 13 of this
 663 manuscript. Supplementary movies are available at link: [LINK](#).

664 **Funding**

665 We acknowledge the Swiss National Science Foundation under grant 178971.

666 **Declaration of Interests**

667 The authors report no conflict of interest.

668 **Author Contributions**

669 A. B., F. V. and F. G. created the research plan. A.B. formulated analytical and numerical
 670 models. A.B. led model solution. A. B. and B. J. designed the experimental setup. B. J.
 671 performed all experiments. A.B., B. J., F.V. and F.G. wrote the manuscript.

REFERENCES

- 672 AFKHAMI, S. & RENARDY, Y. 2013 A volume-of-fluid formulation for the study of co-flowing fluids governed
 673 by the hele-shaw equations. *Phys. Fluids* **25** (8), 082001.
- 674 BATSON, W., ZOUESHTIAGH, F. & NARAYANAN, R. 2013 The faraday threshold in small cylinders and the
 675 sidewall non-ideality. *J. Fluid Mech.* **729** (496-523), 9.
- 676 BENJAMIN, T. B. & URSELL, F. J. 1954 The stability of the plane free surface of a liquid in vertical periodic
 677 motion. *Proc. R. Soc. Lond. A* **225** (1163), 505–515.
- 678 BLAKE, T. D. 1993 Dynamic contact angle and wetting kinetics. *Wettability*.
- 679 BLAKE, T. D. 2006 The physics of moving wetting lines. *J. Colloid Interface Sci.* **299** (1), 1–13.
- 680 BONGARZONE, A., VIOLA, F., CAMARRI, S. & GALLAIRE, F. 2022 Subharmonic parametric instability in
 681 nearly brimful circular cylinders: a weakly nonlinear analysis. *J. Fluid Mech.* **947**, A24.
- 682 BONGARZONE, A., VIOLA, F. & GALLAIRE, F. 2021 Relaxation of capillary-gravity waves due to contact line
 683 nonlinearity: A projection method. *Chaos* **31** (12), 123124.
- 684 CHUOKE, R. L., MEURS, P. VAN & VAN DER POEL, C. 1959 The instability of slow, immiscible, viscous
 685 liquid-liquid displacements in permeable media. *Trans. Am. Inst.* **216** (01), 188–194.
- 686 COCCIAZO, B., FAETTI, S. & FESTA, C. 1993 Experimental investigation of capillarity effects on surface
 687 gravity waves: non-wetting boundary conditions. *J. Fluid Mech.* **246**, 43–66.
- 688 DOLLET, B., LORENCEAU, É. & GALLAIRE, F. 2020 Transition from exponentially damped to finite-time arrest
 689 liquid oscillations induced by contact line hysteresis. *Phys. Rev. Lett.* **124** (10), 104502.
- 690 DOUADY, S. 1990 Experimental study of the Faraday instability. *J. Fluid Mech.* **221**, 383–409.
- 691 DOUADY, S., FAUVE, S. & THUAL, O. 1989 Oscillatory phase modulation of parametrically forced surface
 692 waves. *EPL* **10** (4), 309.
- 693 DUSSAN, E. B. 1979 On the spreading of liquids on solid surfaces: static and dynamic contact lines. *Ann.
 694 Rev. Fluid Mech.* **11** (1), 371–400.
- 695 ERAL, H. B., MANNETJE, J. C. M. 'T & OH, J. M. 2013 Contact angle hysteresis: a review of fundamentals
 696 and applications. *Colloid Polym. Sci.* **291** (2), 247–260.
- 697 FARADAY, M. 1831 *Phil. Trans.* .
- 698 FAUVE, S., DOUADY, S. & THUAL, O. 1991 Drift instabilities of cellular patterns. *J. Phys. II* **1** (3), 311–322.
- 699 GONDRET, P. & RABAUD, M. 1997 Shear instability of two-fluid parallel flow in a hele-shaw cell. *Phys.
 700 Fluids* **9** (11), 3267–3274.
- 701 HAMRAOUI, A., THURESSON, K., NYLANDER, T. & YAMINSKY, V. 2000 Can a dynamic contact angle be
 702 understood in terms of a friction coefficient? *J. Colloid Interface Sci.* **226** (2), 199–204.
- 703 HOCKING, L. M. 1987 The damping of capillary-gravity waves at a rigid boundary. *J. Fluid Mech.* **179**,
 704 253–266.
- 705 HUH, C. & SCRIVEN, L. E. 1971 Hydrodynamic model of steady movement of a solid/liquid/fluid contact
 706 line. *J. Colloid. Interf. Sci.* **35** (1), 85–101.
- 707 JIANG, L., PERLIN, M. & SCHULTZ, W. W. 2004 Contact-line dynamics and damping for oscillating free
 708 surface flows. *Phys. Fluids* **16** (3), 748–758.
- 709 JOHANSSON, P. & HESS, B. 2018 Molecular origin of contact line friction in dynamic wetting. *Phys. Rev.
 710 Fluids* **3** (7), 074201.
- 711 KALOGIROU, A., MOULPOULOU, E. E. & BOKHOVE, O. 2016 Variational finite element methods for waves
 712 in a hele-shaw tank. *App. Math. Model.* **40** (17-18), 7493–7503.
- 713 KUMAR, K. & TUCKERMAN, L. S. 1994 Parametric instability of the interface between two fluids. *J. Fluid
 714 Mech.* **279**, 49–68.
- 715 LAMB, H. 1993 *Hydrodynamics*. Cambridge University Press.
- 716 LI, J., LI, X., HEN, K., XIE, B. & LIAO, S. 2018a Faraday waves in a hele-shaw cell. *Physics of Fluids* **30** (4),
 717 042106.
- 718 LI, J., LI, X. & LIAO, S. 2019 Stability and hysteresis of faraday waves in hele-shaw cells. *J. Fluid Mech.*
 719 **871**, 694–716.

- 720 Li, X., Li, J., LIAO, S. & CHEN, C. 2018b Effect of depth on the properties of two coupled faraday waves in
721 a hele-shaw cell. *Phys. Fluids* **30** (10), 102103.
- 722 Li, X., Li, X. & LIAO, S. 2016 Pattern transition of two-dimensional faraday waves at an extremely shallow
723 depth. *Sci. China Phys. Mech.* **59**, 1–3.
- 724 Li, X., Xu, D. & LIAO, S. 2014 Observations of highly localized oscillons with multiple crests and troughs.
725 *Phys. Rev. E* **90** (3), 031001.
- 726 Li, X., Yu, Z. & LIAO, S. 2015 Observation of two-dimensional faraday waves in extremely shallow depth.
727 *Phys. Rev. E* **92** (3), 033014.
- 728 LUCHINI, P. & CHARRU, F. 2010 Consistent section-averaged equations of quasi-one-dimensional laminar
729 flow. *J. Fluid Mech.* **656**, 337–341.
- 730 McLEAN, J. W. & SAFFMAN, P. G. 1981 The effect of surface tension on the shape of fingers in a hele-shaw
731 cell. *J. Fluid Mech.* **102**, 455–469.
- 732 MÜLLER, H. W., WITTMER, H., WAGNER, C., ALBERS, J. & KNORR, K. 1997 Analytic stability theory for
733 faraday waves and the observation of the harmonic surface response. *Phys. Rev. Lett.* **78** (12), 2357.
- 734 NAYFEH, A. H. 2008 *Perturbation Methods*. Wiley.
- 735 O. V. VOINOV, OV 1976 Hydrodynamics of wetting. *Fluid Dyn.* **11** (5), 714–721.
- 736 PARK, C.-W. & HOMSY, G. M. 1984 Two-phase displacement in hele shaw cells: theory. *J. Fluid Mech.* **139**,
737 291–308.
- 738 PÉRINET, N., FALCÓN, C., CHERGUI, J., JURIC, D. & SHIN, S. 2016 Hysteretic faraday waves. *Phys. Rev. E*
739 **93** (6), 063114.
- 740 PLOURABOUÉ, F. & HINCH, E. J. 2002 Kelvin–helmholtz instability in a hele-shaw cell. *Phys. Fluids* **14** (3),
741 922–929.
- 742 POPINET, S. 2003 Gerris: a tree-based adaptive solver for the incompressible euler equations in complex
743 geometries. *J. Comp. Physics* **190** (2), 572–600.
- 744 POPINET, S. 2009 An accurate adaptive solver for surface-tension-driven interfacial flows. *J. Comp. Physics*
745 **228** (16), 5838–5866.
- 746 RAJCHENBACH, J. & CLAMOND, D. 2015 Faraday waves: their dispersion relation, nature of bifurcation and
747 wavenumber selection revisited. *J. Fluid Mech.* **777**, R2.
- 748 RAJCHENBACH, J., LEROUX, A. & CLAMOND, D. 2011 New standing solitary waves in water. *Phys. Rev. Lett.*
749 **107** (2), 024502.
- 750 RUYER-QUIL, C. 2001 Inertial corrections to the darcy law in a hele–shaw cell. *Comptes Rendus de l'Académie
751 des Sciences-Series IIB-Mechanics* **329** (5), 337–342.
- 752 SAFFMAN, P. G. & TAYLOR, G. I. 1958 The penetration of a fluid into a porous medium or hele-shaw cell
753 containing a more viscous liquid. *Proc. R. Soc. A: Math. Phys. Eng. Sci.* **245** (1242), 312–329.
- 754 SAN, OMER & STAPLES, ANNE E 2012 An improved model for reduced-order physiological fluid flows. *J.
755 Mech. Med. Biol.* **12** (03), 1250052.
- 756 TING, C.-L. & PERLIN, M. 1995 Boundary conditions in the vicinity of the contact line at a vertically
757 oscillating upright plate: an experimental investigation. *J. Fluid Mech.* **295**, 263–300.
- 758 UBAL, S., GIAVEDONI, M. D. & SAITA, F. A. 2003 A numerical analysis of the influence of the liquid depth
759 on two-dimensional faraday waves. *Phys. Fluids* **15** (10), 3099–3113.
- 760 VIOLA, F., BRUN, P.-T. & GALLAIRE, F. 2018 Capillary hysteresis in sloshing dynamics: a weakly nonlinear
761 analysis. *J. Fluid Mech.* **837**, 788–818.
- 762 VIOLA, F. & GALLAIRE, F. 2018 Theoretical framework to analyze the combined effect of surface tension
763 and viscosity on the damping rate of sloshing waves. *Phys. Rev. Fluids* **3** (9), 094801.
- 764 VIOLA, F., GALLAIRE, F. & DOLLET, B. 2017 Sloshing in a hele-shaw cell: experiments and theory. *J. Fluid
765 Mech.* **831**.
- 766 WOMERSLEY, J. R. 1955 Method for the calculation of velocity, rate of flow and viscous drag in arteries
767 when the pressure gradient is known. *Physiol. J.* **127** (3), 553.
- 768 XIA, Y. & STEEN, P. H. 2018 Moving contact-line mobility measured. *J. Fluid Mech.* **841**, 767–783.